

pubs.acs.org/synthbio Research Article

Design of a Genetically Programmable and Customizable Protein Scaffolding System for the Hierarchical Assembly of Robust, Functional Macroscale Materials

Published as part of ACS Synthetic Biology special issue "Materials Design by Synthetic Biology".

Ruijie Zhang, Sun-Young Kang, François Gaascht, Eliana L. Peña, and Claudia Schmidt-Dannert*



Cite This: ACS Synth. Biol. 2024, 13, 3724–3745



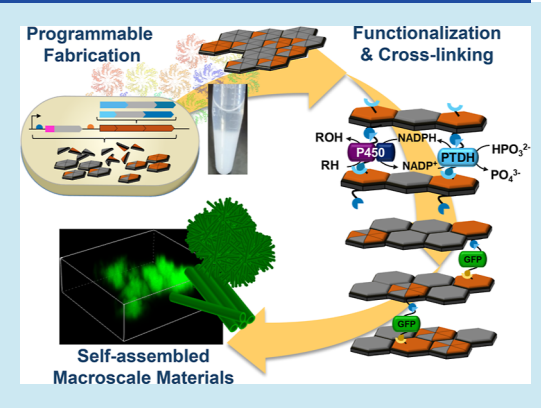
ACCESS

III Metrics & More

Article Recommendations

Supporting Information

ABSTRACT: Inspired by the properties of natural protein-based biomaterials, protein nanomaterials are increasingly designed with natural or engineered peptides or with protein building blocks. Few examples describe the design of functional protein-based materials for biotechnological applications that can be readily manufactured, are amenable to functionalization, and exhibit robust assembly properties for macroscale material formation. Here, we designed a protein-scaffolding system that self-assembles into robust, macroscale materials suitable for in vitro cell-free applications. By controlling the coexpression in *Escherichia coli* of self-assembling scaffold building blocks with and without modifications for covalent attachment of cross-linking cargo proteins, hybrid scaffolds with spatially organized conjugation sites are overproduced that can be readily isolated. Cargo proteins, including enzymes, are rapidly cross-linked onto scaffolds for the formation of functional materials. We show that these



materials can be used for the in vitro operation of a coimmobilized two-enzyme reaction and that the protein material can be recovered and reused. We believe that this work will provide a versatile platform for the design and scalable production of functional materials with customizable properties and the robustness required for biotechnological applications.

KEYWORDS: self-assembly, protein nanomaterials, biomanufacturing, biomaterials, biocatalysis, synthetic biology

■ INTRODUCTION

The chemical and structural variability of proteins makes them ideal building blocks for the design of functional materials that can be genetically programmed and recombinantly manufactured. Numerous protein-based materials are known in nature, many with functions and multiscale assembly properties that are unmatched by human-made, synthetic materials. Materials like silk, elastin, or collagen therefore have inspired the design of synthetic peptide-based materials that have long been studied for biomedical applications. 1-4 Increasingly, selfassembling protein nanomaterials are created from natural or designed peptides and protein domains by leveraging a fastgrowing knowledge base on such building blocks and advances in de novo protein design. 5-10 Significantly fewer examples describe the design of functional protein-based materials for biotechnological applications that can be readily manufactured, are amenable to easy functionalization with multiple, different cargo proteins, and exhibit robust assembly properties for macroscale material formation for operational stability and reuse, e.g., in enzyme reactors for biocatalysis applications. The development of new types of materials for enzyme immobilization in particular is of significant commercial interest. 11 Toward the fabrication of such materials, we

previously showed that the bacterial microcompartment shell protein EutM¹² self-assembles into highly robust, hexameric two-dimensional scaffolds with large surface areas that can be readily produced and isolated from recombinant *Escherichia coli*. ¹³ Scaffold building blocks can also be genetically modified for scaffold surface functionalization with a SpyCatcher domain to allow for rapid covalent attachment of SpyTag modified cargo proteins to scaffolds via isopeptide bond formation. ^{14,15} We then created a toolbox of EutM homologues for the assembly of scaffolds, including hybrid scaffolds from two homologues, with different morphologies and surface properties. ¹⁴ Sampling the different assembly properties as well as the diverse electrostatic surface properties afforded by this EutM toolbox could lead to custom materials with optimized architectures and hexameric arrays with tailored surface

Received: August 27, 2024
Revised: October 7, 2024
Accepted: October 15, 2024
Published: October 31, 2024





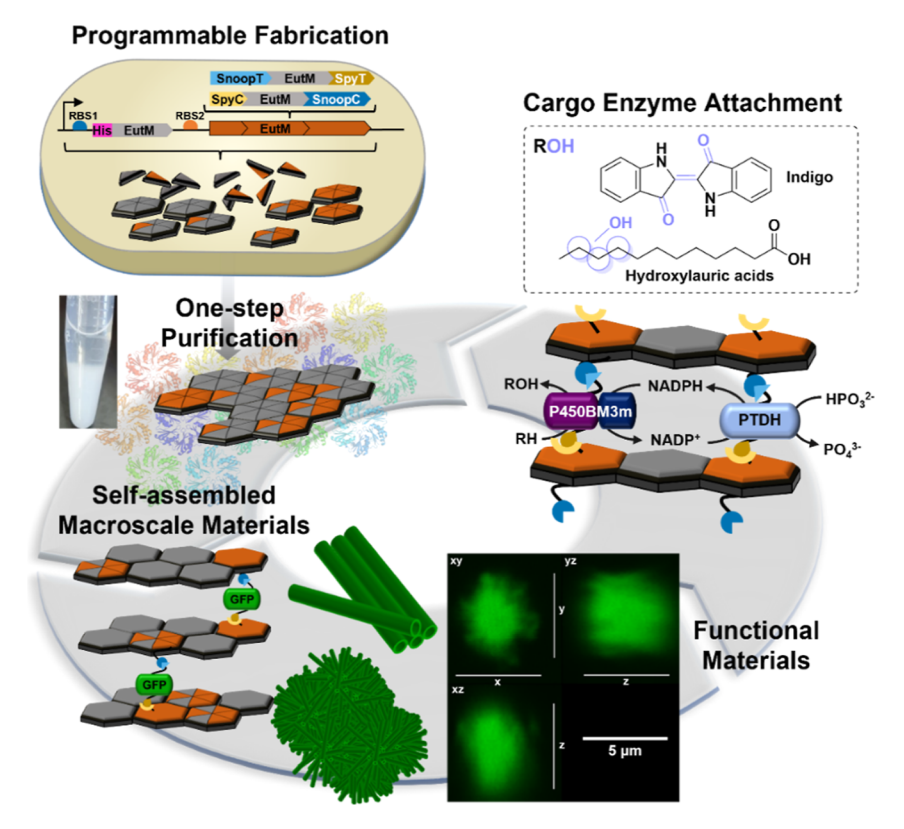


Figure 1. Fabrication of programmable self-assembling functional materials. *E. coli* is engineered for the programmable coexpression of unmodified, His-tagged and dual-modified EutM scaffold building blocks that self-assemble into hybrid scaffolds. A one-step purification yields macroscale scaffolds with controllable building block ratios. Scaffolds can then be cross-linked via isopeptide formation between Spy/SnoopTag (SpyT and SnoopT) and Catcher (SpyC and SnoopC) moieties fused to EutM scaffold building blocks (SnoopT-EutM-SpyT or SpyC-EutM-SnoopC) and cargo proteins of choice as shown for GFP (SnoopC-GFP-SpyC or SpyT-GFP-SnoopT). Finally, the utility of the designed system for the assembly of functional materials is demonstrated with the coimmobilization of a dual-enzyme system composed of a complex, multidomain P450 enzyme (P450BM3m) and a phosphite dehydrogenase (PTDH) for cofactor recycling.

properties for specific applications such as for enzyme reactions. Finally, we used our scaffolds for enzyme immobilization and demonstrated that scaffold attachment increased enzyme stability and efficiency of an enzyme cascade reaction. ^{14,16}

The ease with which our scaffolds can be produced and assembled into robust and highly stable materials that can be modified to enhance the efficiency of biocatalytic reactions, along with diversity of different EutM building blocks available for future design efforts, prompted us to further develop this versatile scaffolding system for the programmable, hierarchical assembly of scaffolds into macroscale, functional materials, as illustrated in Figure 1. To achieve higher-order assembly, we expanded our previously used SpyTag/SpyCatcher (SpyT/ SpyC hereafter) approach covalent scaffold attachment of cargo proteins with the orthogonal SnoopTag/SnoopCatcher (SnoopT/SnoopC hereafter) system for isopeptide bond formation, which has been successfully used to directly crosslink proteins to create polyproteins. ¹⁷ We envisioned that fusion of these orthogonal Tag/Catcher sequences to the N and C termini of EutM scaffold building blocks and cargo proteins of choice will allow cross-linking of scaffolds between cognate Tag and Catcher moieties. Considering our goal of creating functional materials, we envision that bioconjugated cargo proteins can be structural, cross-linking, and/or functional (e.g., enzymes for biocatalysis) components of the assembled, macroscale material where their spatial arrangement is controllable by the density of Tag/Catcher attachment

points on the scaffolds. To prototype our envisioned platform, we first designed and characterized scaffold building blocks that upon bioconjugation with double-tagged GFP as model cargo protein drive the in vitro self-organization of higherordered assemblies. A similar approach has recently been used for the 3D assembly of S-layer sheets. 18 For ease of future scaffold fabrication and to control the density of attachment points, we then demonstrated that by controlling the coexpression of Tag/Catcher fused and unmodified scaffold building blocks in E. coli, we can produce "hybrid" scaffolds with different building block ratios. A one-step purification approach allowed the isolation of these preconfigured hybrid scaffolds for subsequent attachment of cargo proteins for crosslinking into higher-order assemblies and for functionalization. We observed that hybrid scaffolds assemble as arrays of nanotubes under a range of conditions. Importantly, doubletagged GFP could readily be conjugated to these preformed scaffolds and yielded macroscale materials of cross-linked and stacked microtubes that organized into clusters or radial scaffold particles.

To show the applied utility of our system, we then confirmed that GFP can be replaced by cargo enzymes without compromising scaffold cross-linking and assembly, as well as activity of the bioconjugated enzymes. We chose to attach a challenging yet for biocatalysis widely investigated multidomain cytochrome P450 enzyme (P450BM3) and validated its function in concert with a second, coimmobilized enzyme, PTDH for cofactor recycling. 19,20

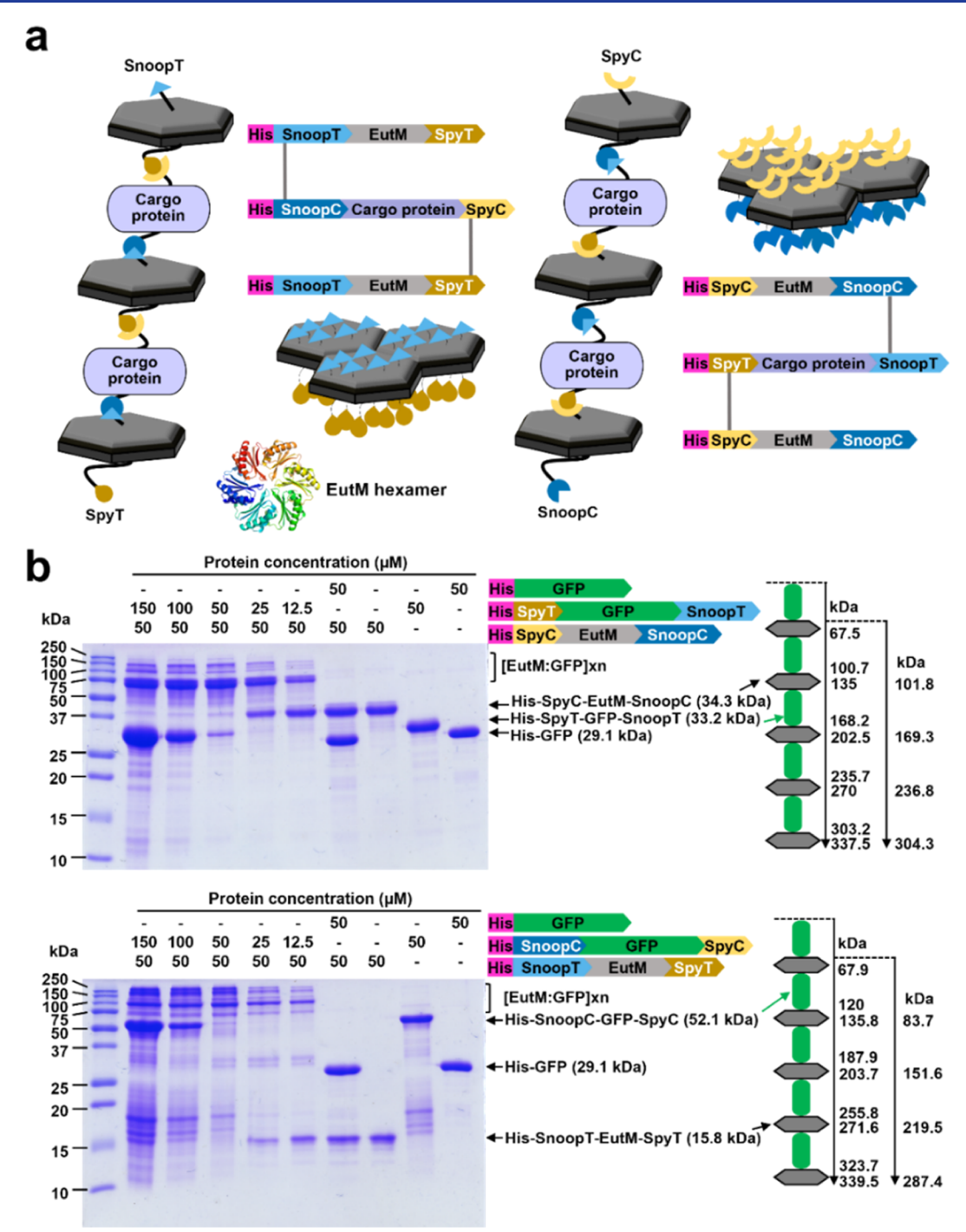


Figure 2. Design and testing of scaffold building block cross-linking. (a) EutM scaffold building blocks self-assemble into hexamers that then assemble into larger scaffolds. Cross-linking of scaffold building blocks is achieved with N- and C-terminal fusion of SpyCatcher/Tag (SpyC and SpyT) and SnoopCatcher/Tag (SnoopC and SnoopT) moieties to EutM and cargo proteins. Isopeptide bond formation (gray line) between cognate Spy/Snoop Catcher/Tag pairs allows for directional linkages shown for the two types of EutM building blocks designed in this work. The illustration shows one out of six conjugation sites per EutM hexamer. (b) Cross-linking of EutM building blocks with GFP was analyzed by SDS-PAGE. Purified His-SpyC-EutM-SnoopC or His-SnoopT-EutM-SpyT was mixed with GFP with or without (control) cognate Catcher/Tag fusions at the molar concentrations shown. Proteins were incubated in 0.1 M sodium phosphate buffer (pH 7.0) at 25 °C for 1 h prior to analysis. Expected molecular weights for one and multiple cross-linked GFP-EutM units are shown to the right. Higher molecular weight bands >67 kDa corresponding to EutM-GFP conjugates form only with dual-modified GFP, with the majority of the GFP conjugated to EutM at a 1:1 molar ratio. Note that less intense bands in the higher concentrated, cross-linked samples represent minor impurities also present in the single protein controls. The shown data are representative for one set of purified proteins.

Despite decades of research dedicated to enzyme immobilization for biocatalytic process development, significant challenges remain in developing strategies that are cost-effective and especially, allow for the immobilization of

multienzyme systems without loss of activities due to incompatible conjugation methods and supports. ¹¹ Bioinspired protein-based bioconjugation and compartmentalization strategies are therefore increasingly explored to address these

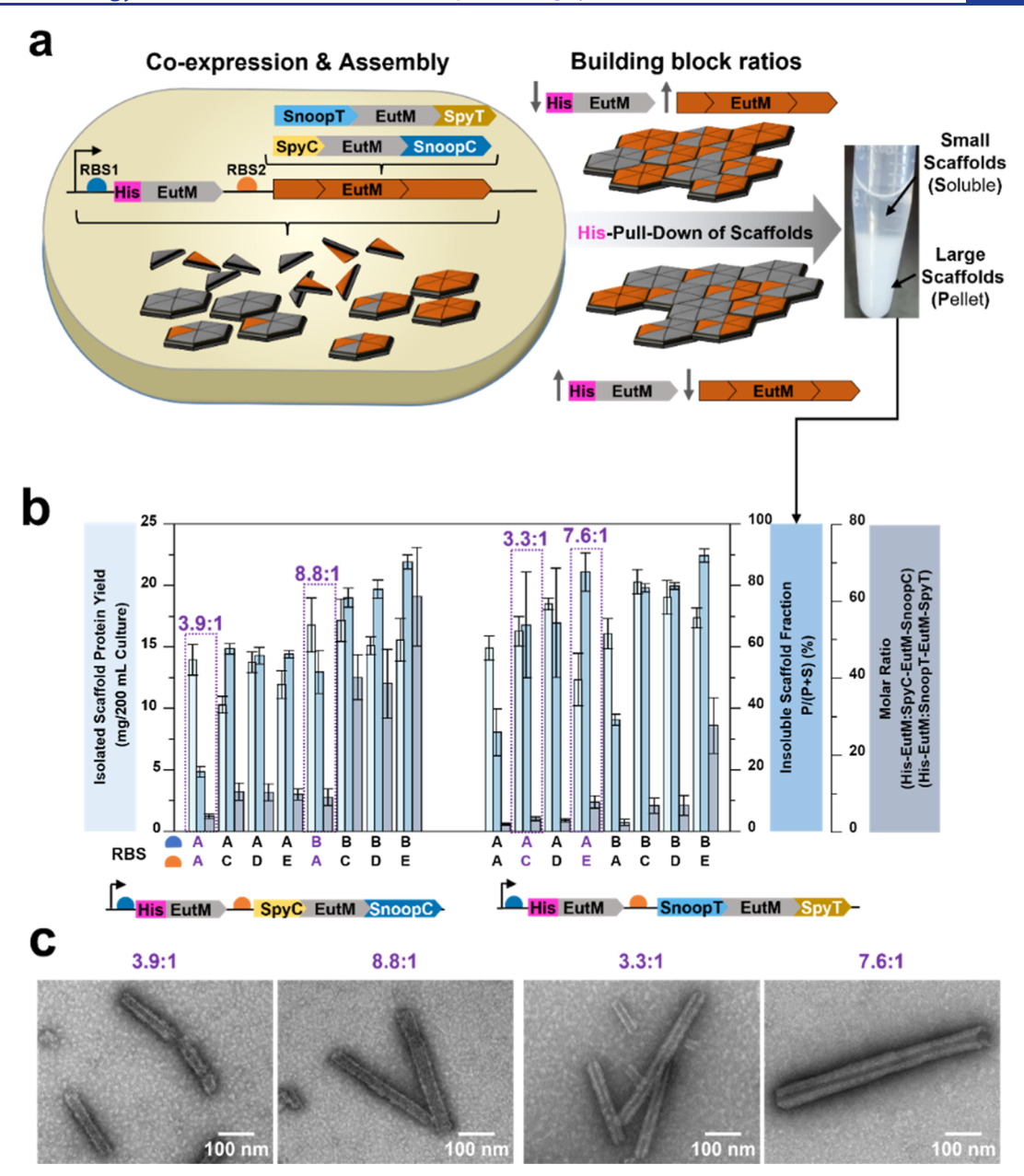


Figure 3. Production and characterization of macroscale hybrid scaffolds. (a) Coexpression of unmodified and dual-modified EutM in E. coli results in the self-assembly of hybrid scaffolds (illustrated as arrays of hexamers). By varying the expression levels of EutM building blocks with ribosome binding sites (RBSs) of different strengths, hybrid scaffolds with different molar ratios of building blocks are produced. Hybrid scaffolds can be selectively pulled-down by His-tag affinity purification, yielding scaffolds that separate into a soluble fraction (S) composed of smaller scaffolds and an insoluble fraction (pellet, P). Shown are the coexpression results for constructs where the His-tag is on the unmodified EutM. Figure S5 shows results for the same constructs where the dual-modified EutMs contain the His-tag. (b) Characterization of hybrid scaffolds coassembled from His-EutM and dual-modified EutM. Eight RBS combinations (RBS A-E) were used to vary scaffold building block ratios. Scaffolds were purified from 200 mL cultures in the presence of 4 M urea and the total yield of isolated scaffolds was quantified. The percentage of the insoluble scaffold fraction of normalized scaffolds (2 mg/mL) (as an indicator of assembly strength) was determined after dialysis into 0.1 M Tris-HCl buffer (pH 7.5) to remove urea. The molar ratios between EutM building blocks of the isolated hybrid scaffolds were analyzed by SDS-PAGE densitometry. Two hybrid scaffolds (purple boxes and fonts) for each of the two building block combinations with comparable molar ratios were selected for further studies. Data are shown as mean values ±SD and error bars represent the standard deviations of replicates from three independent cultures for each expression construct. Figure S6 shows representative SDS-PAGE gels used for analysis. (c) Selected hybrid scaffolds were analyzed by TEM after dialysis into 0.1 M sodium phosphate buffer (pH 7.0) and dilution to 1 mg/mL. Shown are the representative images of scaffolds captured at 60k× magnification [see Figure S7 for additional images and magnifications (10k-120k×)]. Arrays of hexamers depicted in (a) appear to roll up into tubes to create the scaffolds observed by TEM.

issues. ^{2,3,8,14,18,21-27} But in most of these studies, model enzyme systems or materials that lack robustness, modularity, and versatility as well as macroscale assembly properties are used for in vitro applications. This limits their utility for the

development of industrial processes that require inexpensive, easy to use, and tailorable systems and materials that are stable and can be reused. We believe this work will add to the current landscape of genetically engineered materials by providing a platform for the design of robust and customizable materials that can be easily manufactured recombinantly for a multitude of applications. In addition, unlike traditional, synthetic materials, these protein-based materials are biodegradable, therefore increasing the sustainability of industrial processes such as, e.g., for biocatalysis—which is becoming increasingly important.²⁸

RESULTS AND DISCUSSION

Design and Characterization of Building Blocks for Scaffold Assembly. We first modified our EutM scaffolds to allow not only for the immobilization of biocatalysts 14,16 but also the formation of larger and more complex structures without impeding scaffold assembly. For this, we used the efficient SpyCatcher/Tag system together with the similar SnoopCatcher/Tag system¹⁷ for isopeptide-mediated crosslinking of double-tagged EutM scaffolds and cargo proteins with cognate tags into assemblies (Figure 2a). Previously, we found that the fusion of the larger SpyC domain is tolerated by EutM scaffolds, while fusion of this domain to cargo enzyme can negatively affect their activity. 14,16 We therefore designed two opposite configurations with either the smaller Tags (SpyT = 1.4 kDa and SnoopT = 1.5 kDa) or larger Catcher (SpyC = 9.1 kDa and SnoopC = 12.6 kDa) moieties fused to the N and C termini of EutM. We chose to design doubleinstead of single- N- or C-terminal-tagged EutM building blocks to create an easier to control scaffolding system.

As a model cargo protein for characterization of scaffold building block cross-linking and for subsequent visualization, we engineered monomeric sfGFP²⁹ with corresponding fusions. For one-step nickel affinity purification, an N-terminal His-tag was added to the two EutM scaffold building blocks (His-SnoopT-EutM-SpyT and His-SpyC-EutM-SnoopC) and GFP cargo proteins (His-SpyT-GFP-SnoopT and His-SnoopC-GFP-SpyC). Note that while the C terminus of EutM is assumed to be located on the concave site ("bottom" side) of the hexamer based on structural information (PDB accession number 3I6P), we presume that the N-terminal fusions due to steric hindrances are located on the opposing site of the hexamer, as depicted in Figure 2a. In the crystal structure, the N terminus of EutM is close to the hexamer interface, and fusions, especially with a flexible linker used in our designs (Table S4), could therefore be displayed on the convex ("top") site. Labeling of His-SpyC-EutM-SnoopC bound to metal-affinity beads SpyT/SnoopT-tagged GFP and mCherry indicates that this may be the case (Figure S1).

Both dual-modified EutM building blocks could be readily overproduced and isolated from E. coli. We noticed though that the two purified proteins were much more soluble than our previously characterized His-EutM-SpyC and His-EutM. 13,14,16 The Catcher-modified His-SpyC-EutM-SnoopC remained soluble at >20 mg/mL, while the Snoop/SpyTmodified His-SnoopT-EutM-SpyT precipitated out of solution at ~5 mg/mL. No large structures were observed for either protein by transmission electron microscopy (TEM). In contrast, as observed previously, 13,14,16 His-EutM assembles into hexameric rolled-up or flat scaffolds that precipitate out at 2 mg/mL, while the more soluble His-EutM-SpyC scaffolds out of solution at >5 mg/mL as assemblies of long fibril-like structures. 13,14 All EutM building block purifications were performed in the presence of 4 M urea for scaffold solubilization to maximize protein yield as described previously. 13,14 Removal of urea causes the reformation of

insoluble scaffolds (visible as a white pellet; see Figure 3a) except for the highly soluble His-SpyC-EutM-SnoopC scaffold building block. Native PAGE analysis of scaffolds solubilized in urea (Figure S2a) and after removal of urea (Figure S2b) shows similar higher molecular weight assemblies of ~400-800 kDa in size for each dual-modified building block, suggesting that scaffolds able to migrate into the gel form the same stable assemblies under both conditions. The assemblies appear to be composed of two (His-SpyC-EutM-SnoopC) or eight (His-SnoopT-EutM-SpyT) hexamers based on their molecular weights (Figure S2c). For comparison, His-EutM scaffolds seem to be assembled from six hexamers (Figure S2a-c). Surprisingly, we did not observe a band with a size corresponding to a single hexamer, which was the major band obtained for the bacterial microcompartment shell protein (RmmH) from Mycobacterium smegmatis. 30 It appears that the N- and C-terminal fusions added to EutM do not affect monomer assembly into hexamers but rather the assembly into larger scaffolds observed for His-EutM.¹

With scaffold self-assembly of the dual-modified EutM building blocks confirmed, we next investigated their covalent cross-linking with the corresponding dual-modified GFP fusion proteins (Figures 2b and S3). Mixing of the modified EutM building blocks with their cognate GFP fusion protein partners at different molar ratios results in rapid cross-linking that is complete within 1 h based on SDS-PAGE analysis. As we have observed previously for EutM-SpyC, a small amount of Catcher-modified EutM or GFP remained unconjugated regardless of molar ratios, incubation time, or temperature (Figures 2b and S3), suggesting that their Catcher domains are not in a competent state for peptide bond formation. Crosslinking progressed from one EutM monomer conjugated with one GFP to four or more EutM cross-linked by GFPs to create larger assemblies, including assemblies with molecular weights too large for SDS-PAGE separation. The formation of larger assemblies proceeded over time and seemed to be faster between His-SnoopT-EutM-SpyT and His-SnoopC-GFP-SpyC compared to His-SpyC-EutM-SnoopC and His-SpyT-GFP-SnoopT as observed by changes in SDS-PAGE gel banding patterns over time (Figure S3).

In summary, the Spy/Snoop-Tag/Catcher system proved to be an effective system not only for cargo protein attachment to scaffolds but also for cross-linking of scaffolds into higher molecular weight complexes. Notably, N- and C-terminal fusion of the larger Catcher domains to EutM does not appear to interfere with hexamer assembly, therefore providing versatility for cargo attachment and scaffold cross-linking. Nevertheless, modification of both the N and C termini of EutM impacted assembly into larger, insoluble scaffolds desirable for macroscale material formation.

Coassembly of Scaffold Building Blocks into Macroscale Hybrid Scaffolds. To promote the assembly of larger, insoluble scaffolds, we sought to coassemble hybrid scaffolds from dual-modified and unmodified EutM building blocks. This would then also allow for the spatial distribution of bioconjugation points to control cross-linking and/or cargo attachment. Previously, we found that the spacing of attachment points for enzyme immobilization on EutM-SpyC scaffolds was important for the optimization of biocatalyst activities. However, our first attempt of simply mixing in ureapurified His-EutM and dual-modified His-EutM proteins followed by dialysis (for scaffold formation) did not yield the desired coassembled hybrid scaffolds (Figures S2 and S4).

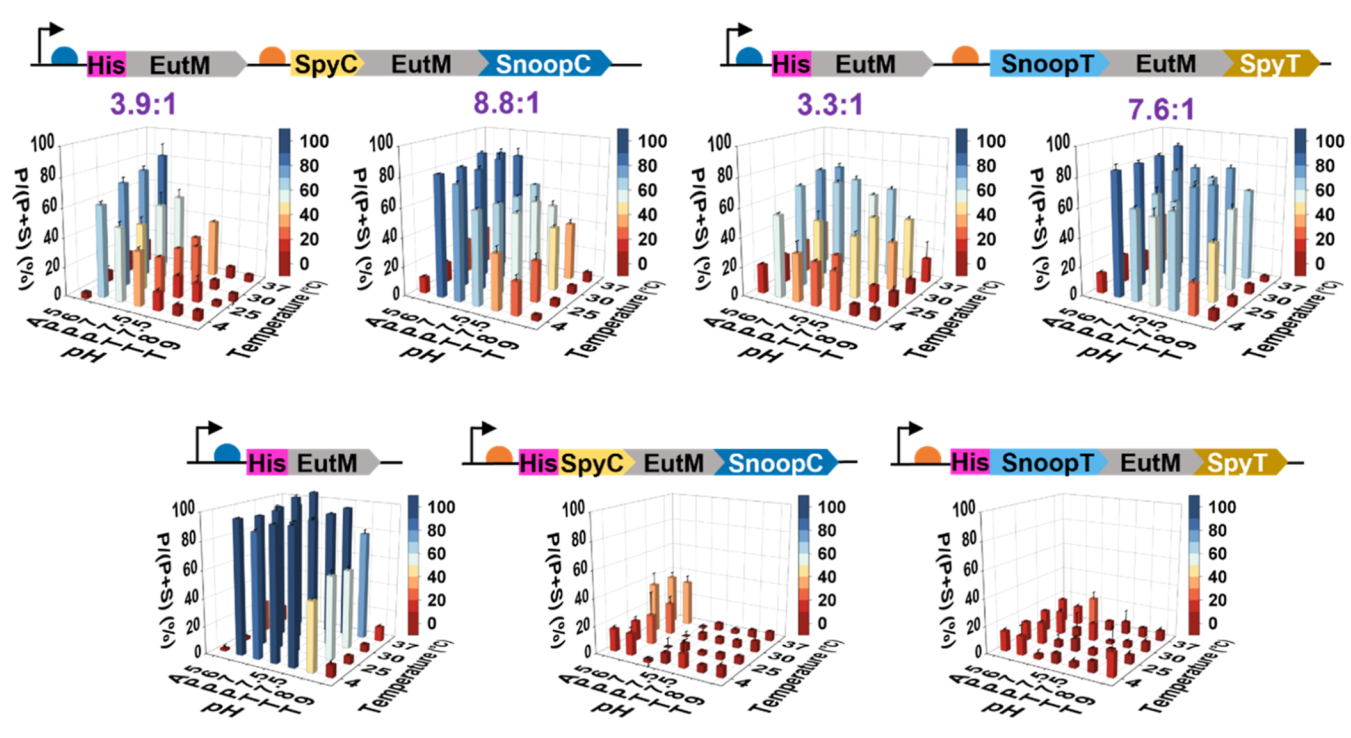


Figure 4. Characterization of scaffold assembly strength. Four hybrid scaffolds with different molar ratios (purple numbers) of coexpressed unmodified and dual-modified EutM building blocks were selected for characterization of assembly strength and compared to scaffolds formed by individual building blocks. Scaffolds (3 mg/mL in urea) were dialyzed into buffers with different pH values, normalized to 2 mg/mL, and then incubated for 24 h at different temperatures. The percentage of the insoluble scaffold (P) fraction relative to the combined amount of soluble (S) and insoluble scaffold (P) [P/(P+S)] as in Figure 3 was then calculated as an indicator of assembly strength. The following buffers were used: 0.1 M sodium acetate (A, pH 5), 0.1 M sodium phosphate (P, pH 6, 7, or 7.5), and 0.1 M Tris-HCl (T, pH 7.5, 8, or 9). The same experiments were also conducted with 0.1 and 0.25 M NaCl added to buffers (Figures S8 and S9). Data are shown as mean values \pm SD and error bars represent the standard deviations of three independent experiments per scaffold.

Instead, each building block retained similar soluble assemblies as those observed for the individual blocks (Figure S2). In addition, the dual-modified building blocks remained largely in the soluble fraction after urea removal, while the unmodified EutM scaffolded out of solution (Figure S4). EutM monomers must therefore quickly self-assemble into stable multimeric units (e.g., as hexamers and/or multiple hexamers) that cannot be disassembled and reconfigured once expressed in *E. coli* and after solubilization in urea.

To overcome this coassembly problem, we designed coexpression constructs for E. coli where individual building block expression levels are controlled by RBSs with different strengths (Figure 3). We chose five different RBSs (Table S1) for coexpression of EutM and double-tagged EutM under the control of a cumate-inducible promoter. 14,31-34 Only one of the coexpressed building blocks contains an N-terminal His-tag (Figure 3b shows the His-EutM designs and Figure S5 the opposite designs), allowing for the pull-down of only hybrid scaffolds, an approach that we have used to confirm the coassembly of EutM homologues from different bacteria. 14 Depending on building block expression levels, we expected to obtain hybrid scaffolds with different EutM building block molar ratios. A higher ratio of unmodified EutM was anticipated to increase the fraction of larger scaffolds that pellet out of solution, as illustrated in Figure 3a.

We designed twenty-nine EutM coexpression constructs with different RBS combinations for each of the two dual EutM building blocks and the His-tag placed either on EutM or the modified EutMs (Figures 3b and S5). We then comprehensively characterized protein yield, scaffold assembly

behavior (i.e., formation of large, insoluble scaffolds), and molar ratio of EutM to dual-modified EutM building blocks in the hybrid scaffolds (Figures 3b and S5). Scaffold production yields and molar ratios of scaffold building blocks were determined directly after nickel affinity purification pull-down in urea by measuring protein concentrations and by SDS-PAGE densitometry (Figure S6). Assembly behavior was compared by normalizing the concentration of all purified scaffolds in urea first to ~2 mg/mL prior to dialysis into 0.1 M Tris-HCl pH 7.5 buffer for assembly into larger scaffolds. Insoluble scaffolds were then separated from the soluble assemblies by centrifugation. Quantification of proteins in each fraction yielded the percentage of insoluble scaffold material formed, as an indicator of assembly strength.

We found that scaffold yields, as well as the molar ratios of building blocks, varied significantly across designs with no strong correlations between RBS combinations (Figure 3b). Notably, scaffold yields were much lower for the designs where the His-tag was on the modified EutM building blocks because of its lower expression levels (Figure S5). Consequently, we chose to proceed only with the His-EutM-containing hybrid scaffolds shown in Figure 3b that are readily overproduced in E. coli. For these hybrid scaffolds, the ratios between EutM and dual-modified EutM ranged from 1.9:1 to 61:1, therefore providing options for creating scaffolds with different densities of bioconjugation sites. As expected, higher molar ratios of unmodified EutM increased the formation of larger, insoluble scaffolds for all hybrid scaffold coexpression designs. Likewise, hybrid scaffolds with SnoopT-EutM-SpyT showed stronger assembly into larger, insoluble scaffolds compared to those

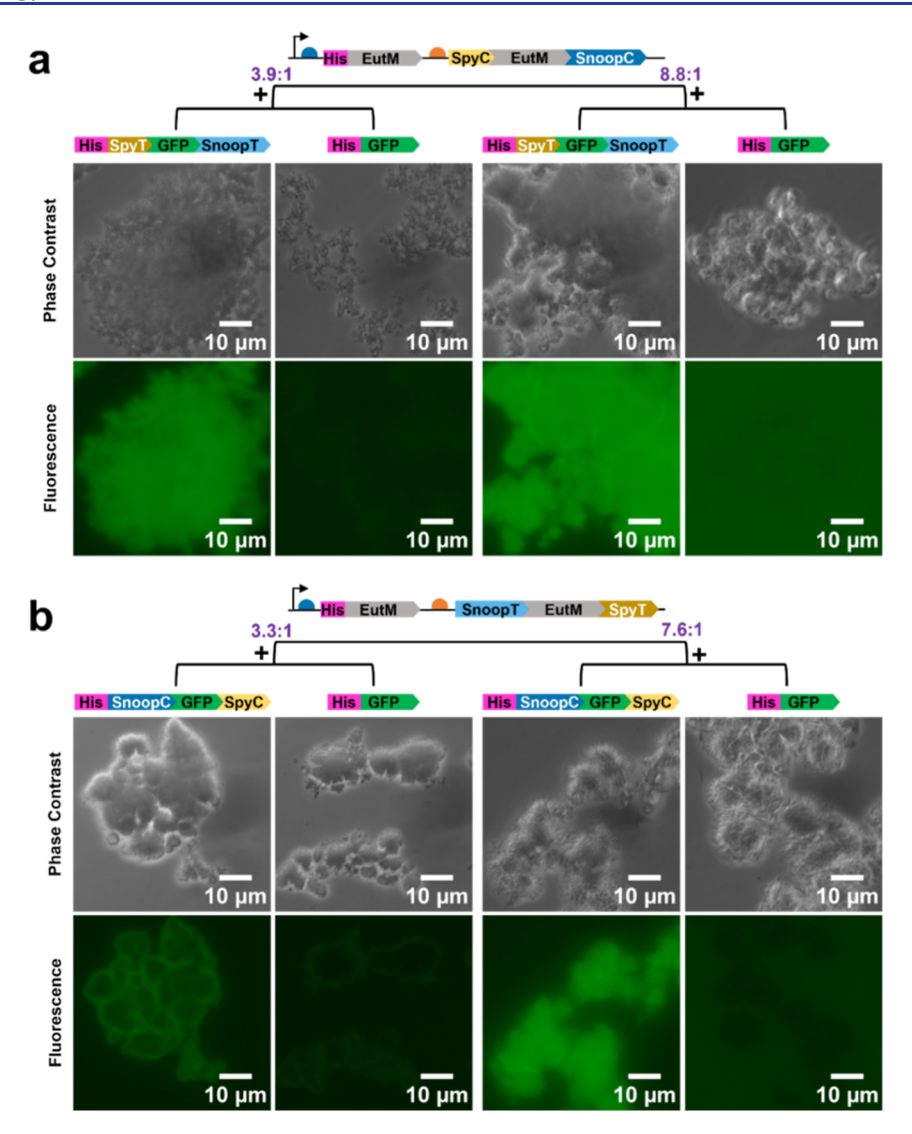


Figure 5. Imaging of hybrid scaffold structures and GFP attachment. (a) His-EutM:SpyC-EutM-SnoopC hybrid scaffolds (molar ratios of 3.9:1 and 8.8:1 from Figure 3) were mixed with either His-SpyT-GFP-SnoopT or unmodified (control) His-GFP cargo proteins to observe scaffold structures and GFP cargo attachment. Scaffolds are visible as macroscale materials that appear more compact for His-EutM:SpyC-EutM-SnoopC = 8.8:1 hybrid scaffolds that contain a higher ratio of unmodified EutM. GFP attachment to scaffolds is only observed with tagged GFP cargo. (b) His-EutM:SnoopT-EutM-SpyT hybrid scaffolds (molar ratios of 3.3:1 and 7.6:1 from Figure 3) were mixed with His-SnoopC-GFP-SpyC or unmodified (control) His-GFP cargo protein. Both hybrid scaffolds form macroscale materials visible as dense structures with radial microtube assemblies that are more pronounced for the His-EutM:SnoopT-EutM-SpyT = 7.6:1 hybrid scaffolds. GFP cargo attachment is only observed with the Catchermodified GFP cargo. Experiments were performed by mixing 50 μ M GFP cargo in 0.1 M sodium phosphate buffer (pH 7.0) with hybrid scaffolds such that the concentrations of their modified EutM building blocks are equimolar to that of their cognate GFP cargo partner (see Methods for protein concentrations). After incubation for 1 h at 25 °C and 180 rpm, samples were prepared for imaging. Representative images from one set of purified proteins are shown. Additional images, including for different GFP cargo ratios, are provided in Figures S11 and S13.

containing the Catcher-modified EutM building block. The Snoop/SpyTag fusions are much smaller than the Catcher domains and therefore presumably have less of an impact on scaffold assembly, thus, resulting in the formation of larger scaffolds.

Two designs from each hybrid scaffold type with either SpyC/SnoopC or SnoopT/SpyT conjugation sites were then selected for additional characterization and cross-linking studies (Figure 3b, purple boxes). The molar building block ratios of these four scaffolds range from approximately 3:1 to 9:1, providing a density of conjugation sites comparable to ratios that we previously confirmed to work well for enzyme immobilization on EutM-SpyC scaffolds.¹⁴ In addition, these scaffold constructs (from here on referred to by their molar

ratios: 3.9:1, 8.8:1, 3.3:1, and 7.6:1) afford the isolation of insoluble hybrid scaffolds at good yields from recombinant *E. coli* cells. Importantly, TEM confirms that all four hybrid scaffolds self-assemble into well-ordered structures composed of long, hollow rolled-up nanotubes with diameters ranging from 25 to 60 nm that appear similar to structures observed for His-EutM scaffolds ^{13,14,16} (Figures 3c and S7). Nanotube walls appear to be thicker and multilayered for the SnoopT-EutM-SpyT containing hybrid scaffolds, with more pronounced layering, striations, and larger nanotube diameters for the His-EutM:SnoopT-EutM-SpyT = 7.6:1 hybrid scaffold which contains a higher molar ratio of unmodified EutM (Figure S7). The single-layered nanotubes look very similar to those reported for the bacterial microcompartment shell protein

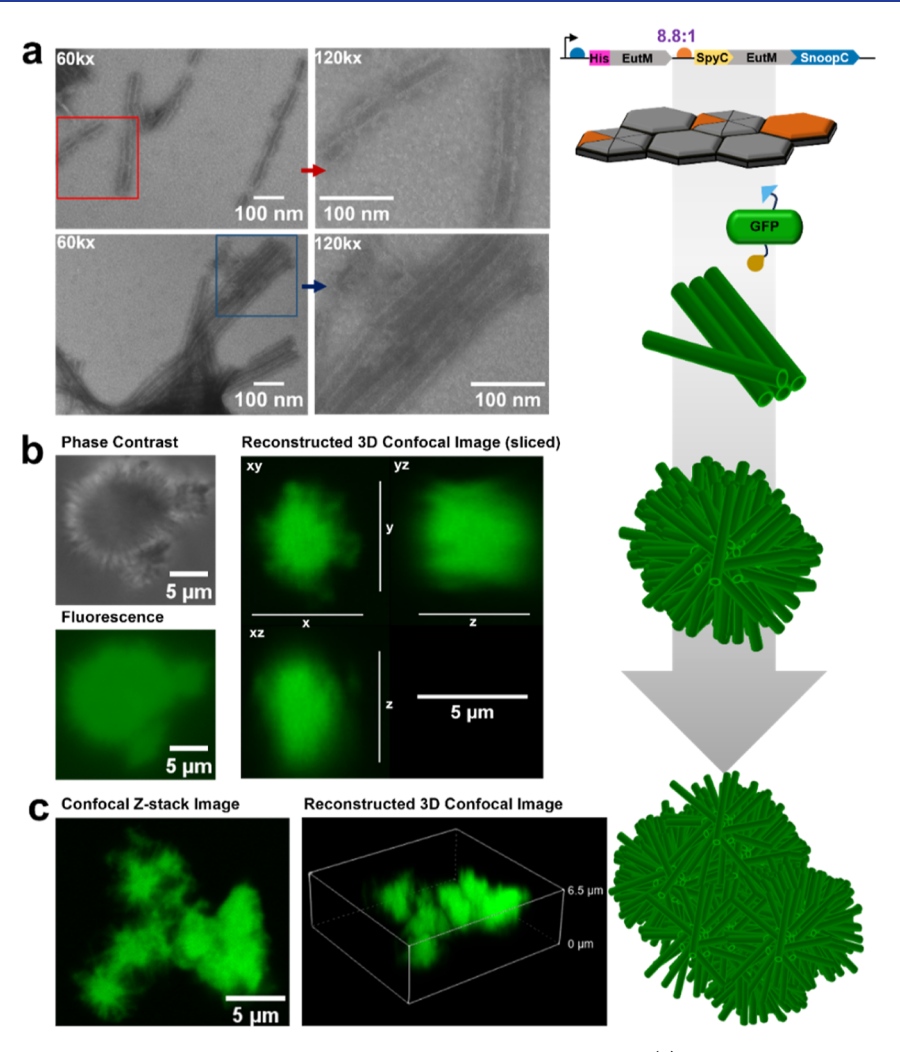


Figure 6. High-resolution microscopy imaging of GFP cross-linked hybrid scaffold assemblies. (a) TEM of hybrid His-EutM:SpyC-EutM-SnoopC = 8.8:1 scaffolds with cross-linked His-SpyT-GFP-SnoopT cargo (see Figure 5a) shows EutM scaffold nanofibers that appear to be coated (red arrows) with GFP compared to the thinner and more articulated tube-like scaffold structures observed in Figure 3c. Bundles of fibers are observed that are enveloped by a film (blue arrows), suggesting cross-linking by the dual-modified GFP. Parallel and radially aligned fiber bundles can be observed that are reminiscent of the radial structures observed by light microscopy (see Figure S14 for additional TEM images and magnifications). Red and blue boxes mark areas further magnified to the right. Samples are diluted to 1 mg/mL for TEM analysis. Representative images from one set of proteins are shown. (b) Phase contrast and confocal fluorescence microscopy of a single, radial scaffold particle and a larger scaffold assembly composed of clusters of radial particles from the same GFP-cross-linked hybrid scaffolds imaged by TEM. Images show the micrometer dimensions of the scaffolds. Confocal Z-stack imaging shows GFP fluorescence across the entire scaffold structures. (c) Imaging results suggest a scaffold-assembling process that starts with the assembly of EutM hexamers into microtubes which form radial, microscale particles that are coated and cross-linked with GFP. Particles and bundles of microtubes cluster together into larger microscale scaffolds observed by microscopy and eventually form the large insoluble macroscale materials that fall out of solution.

RmmH from *M. smegmatis*,³⁰ while the thicker tubes are more similar to the structures we have previously observed for EutM homologues.¹⁴ Note that TEM analysis required dilution of scaffolds to 1 mg/mL to prevent grid breakage and allow for imaging of individual structures.

Controlling the coexpression of scaffold building blocks therefore is a simple approach to produce scaffolds with different assembly properties, which is also amenable to future scale-up.

Characterization of Hybrid Scaffold Assembly Stability. Protein self-assembly, including the assembly of microcompartment shell proteins like EutM, is dynamic and dependent on environmental conditions such as protein concentration, pH, salts, and temperature. The usefulness of our scaffolds for different applications, such as biocatalysis, will depend on their stable assembly across a range of

commonly used conditions. We therefore investigated the influence of buffers (pH 5.0-9.0), temperatures (4, 25, 30, and 37 °C) (Figure 4), and salt (100 and 250 mM NaCl) (Figures S8 and S9) on their assembly stability by quantifying the percentage of insoluble scaffolds after 24 h incubation. For comparison, we also assessed the assembly stability of the individual scaffold building blocks under the same conditions.

Consistent with the observations above, the dual-modified EutM building blocks showed the lowest assembly propensity, while the unmodified EutM protein formed stable, insoluble scaffolds that made up 49–100% of the total protein sample across all conditions except at pH 5.0 and 9.0. The assembly stabilities of the hybrid scaffolds fall in between their constituent building blocks and molar ratios (Figures 4, S8, and S9). Elevated temperatures increased self-assembly stability as we have observed previously for EutM homo-

logues. ^{14,36} Assembly was optimal between pH 6.0 and 7.5, with a preference for neutral pH 7.0 and phosphate instead of Tris-HCl buffers. Variations among scaffolds may be attributed to the different isoelectric points of the building blocks (calculated pI values are His-EutM = 6.7, SpyC-EutM-SnoopC = 5.4, and SnoopT-EutM-SpyT = 7.8). The addition of NaCl slightly decreased scaffold formation, except for the unmodified EutM (Figures S8 and S9).

In summary, these results show that scaffold assembly is retained in conditions relevant for applications such as biocatalysis and that higher EutM building block ratios increase self-assembly stability.

GFP Cargo Attachment and Cross-Linking of Hybrid **Scaffolds.** To test whether our GFP model cargo protein can still be efficiently conjugated to the dense, macroscale materials formed by the hybrid scaffolds, purified scaffolds (20-40 mg/ mL) were incubated with equimolar ratios of dual-modified GFP (unmodified GFP as a control) to the dual-modified EutM building block (50 μ M) in the hybrid scaffolds. After 1 h of incubation, large scaffold structures can be observed by light microscopy that are conjugated with GFP (Figure 5). Testing of different molar ratios of GFP to dual-modified EutM (4:1 to 1:4, with the EutM partner fixed at 50 μ M) demonstrated efficient cross-linking of EutM building blocks with 25-50 µM GFP into higher molecular weight complexes (Figure S10). However, more unbound GFP remained after 1 h incubation with the hybrid scaffolds that have higher unmodified EutM ratios, suggesting that not all conjugation sites are readily accessible in these dense materials.

The morphologies of the hybrid scaffold materials vary, with more dense structures formed with higher ratios of unmodified EutM (His-EutM:SpyC-EutM-SnoopC = 8.8:1 and His-EutM:SnoopT-EutM-SpyT = 7.6:1) (Figure 5, see Figures S11 and S13 for different GFP cargo ratios). Closer inspection of the His-EutM:SpyC-EutM-SnoopC = 8.8:1 and both His-EutM:SnoopT-EutM-SpyT materials (visible at the fringes of the structures) suggests that scaffolds are formed from stacked microtubes that assemble into radial particles that are pronounced in the His-EutM:SnoopT-EutM-SpyT = 7.6:1 scaffolds which are assembled from larger nanotubes (Figure 3c).

To further characterize the structural features of GFPconjugated hybrid scaffolds, we chose cargo-loaded His-EutM:SpyC-EutM-SnoopC = 8.8:1 hybrid scaffolds (Figure 5a) that we would later use for enzyme immobilization for TEM and confocal microscopy imaging (Figures 6 and S14). TEM images indicate that scaffold fibers are coated by GFP compared with the thinner and more articulated fibers observed in Figure 3c. In addition, bundles of fibers are linked together, presumably by the conjugated GFP cargo protein, Figure 6a. Confocal microscopy, including 3D reconstructions, delineates the micrometer dimensions of radial particles that are conjugated throughout with GFP and their clustering into larger scaffolds, Figure 6b, suggesting a scaffold assembling and cross-linking process that involves the hierarchical assembly of microtubes into cross-linked radial particle clusters illustrated in Figure 6c with dimensions that exceed 10 μ M in size. Despite the large size of the particles, we attempted to measure the particle distribution of this sample and a control with untagged GFP (Figure 5a) by dynamic light scattering (DLS). However, the majority of the particles are outside of the range (>10 μ m) for DLS analysis, and measurements of smaller particle distributions in these samples were impeded by beam

reflections caused by the large particles (see the example in Figure S12a). We then performed analytical ultracentrifugation (AUC) to assess the particle size distribution. For consistency, sedimentation velocity experiments were performed again with the same hybrid scaffolds (His-EutM:SpyC-EutM-SnoopC = 8.8:1) and conditions containing His-SpyT-GFP-SnoopT (GFP cross-linked hybrid scaffolds) as in Figures 5a and 6. Because the protein concentrations (50 μ M GFP and 50 μ M modified scaffold building blocks used for the cross-linking experiments) in these samples were not sufficient for determining particle sedimentation coefficients at 280 nm (OD > 0.5 required), measurements were performed at 485 nm corresponding to GFP absorption as a proxy (Figure S12b). Sedimentation velocity analysis showed that 50% of the GFP molecules form higher molecular weight multimers in the GFP cross-linked hybrid scaffold sample. In contrast, the control sample shows a single peak at 2.8 S and a narrow size distribution, suggesting that GFP is mostly free and not bound to EutM scaffolds. The sedimentation coefficient distribution of the GFP cross-linked hybrid scaffolds is more complex due to the formation of multimers with higher sedimentation velocities and a broad size distribution with a peak at 7 S. These results confirm that GFP cross-link hybrid scaffolds are composed of higher molecular weight assemblies as observed by microscopy in Figure 6. Further fluorescence microscopy analysis of these samples [prepared at a 100-fold lower protein concentration (0.1 mg/mL final concentration) than in Figures 5 and 6] and comparison with a similarly prepared sample of scaffolds mixed with GFP-SpyT-His for labeling showed that the cross-linked scaffolds assemble into large ordered arrays (20 to >100 μ m in size) compared to the particle clusters and sheets formed by the scaffolds labeled with the single tagged GFP (Figure S12c).

Testing Hybrid Scaffolds for Enzyme Immobilization. Our results showed that the designed hybrid scaffolds can be readily produced in *E. coli* with configurable conjugation site densities. They are also stable and self-assemble into macroscale materials that are efficiently conjugated and cross-linked with GFP as a model cargo protein. These are useful characteristics for the creation of customizable functional materials for a range of biotechnological applications. As a first step toward the design of such materials, we assessed the utility of our scaffolding system for enzyme immobilization by replacing GFP with two enzymes for the operation of a two-enzyme reaction.

As a proof of concept, we selected the challenging yet extensively studied and highly versatile multidomain cytochrome P450 monooxygenase CYP102A1 known as P450BM3.^{20,37} Unlike many P450 enzymes, P450BM3 can be recombinantly expressed as soluble protein, is self-sufficient due to a fused NADPH reductase domain, and is known to catalyze diverse reactions and over thousand variants have been described. 20,37 Yet, industrial use of this enzyme remains challenging due to its complex, two-domain, and dimeric protein structure and undesired "uncoupling" of NADPHderived electrons to produce reactive and inactivating oxygen species and/or H₂O₂. To improve P450BM3 reaction efficiency and for catalysts and NADPH cofactor recycling, diverse immobilization methods have been developed, including the coimmobilization of P450BM3 with cofactor recycling enzymes. 26,38-43 From this knowledge base, we chose the P450BM3 variant GVQ (A74G, F87V, L188Q) (referred herein as P450BM3m) which oxidizes a range of substrates,

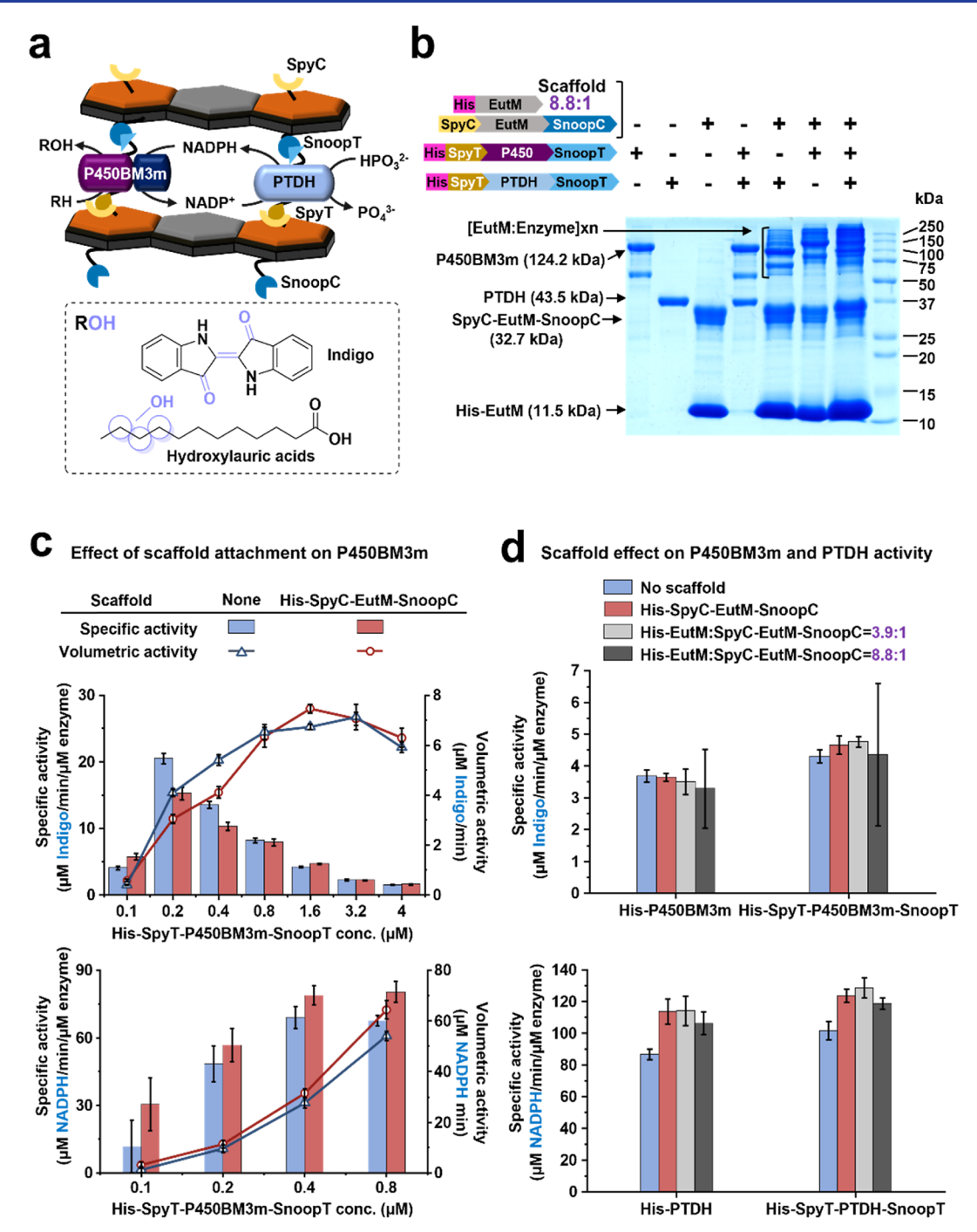


Figure 7. Immobilization of P450BM3m and PTDH onto hybrid EutM scaffolds. (a) P450BM3m and PTDH are coimmobilized onto His-EutM:SpyC-EutM-SnoopC = 8.8:1 hybrid scaffolds via their N- and C-terminal cross-linking SnoopT and SpyT fusions. The resulting immobilized dual-enzyme system facilitates phosphite-driven NADPH cofactor recycling by PTDH for the P450BM3m-catalyzed hydroxylation of indole into indoxyl (which dimerizes into indigo) or of lauric acid into 9-, 10-, and 11-hydroxylauric acids. (b) Confirmation of cross-linking of SpyC-EutM-SnoopC in the His-EutM:SpyC-EutM-SnoopC = 8.8:1 scaffolds with P450BM3m and PTDH. Enzymes were mixed with the hybrid scaffold at a 1:4 molar ratio corresponding to the SpyC-EutM-SnoopC building block in the scaffold. Samples in 0.1 M phosphate buffer (pH 7.0) were incubated for 1 h at 30 °C and 180 rpm prior to SDS-PAGE analysis. Control reactions were performed with and without enzymes and scaffolds as shown. The formation of high molecular weight complexes (as for GFP in Figure 1b) confirms that the cross-linking fusion tags are functional. Results for His-EutM:His-SpyC-EutM-SnoopC = 3.9:1 and His-SpyC-EutM-SnoopC scaffolds are found in Figure S16. (c) Effects of N- and Cterminal cross-linking of His-SpyT-P450BM3m-SnoopT to scaffolds on enzyme activity were determined by mixing the enzyme with His-SpyC-EutM-SnoopC at a 1:4 molar ratio in 0.1 M phosphate buffer (pH 7.0). After dilution to achieve different molar enzyme concentrations (0.5-20 μ M), samples were incubated for 1 h at 30 °C to allow for isopeptide bond formation. Specific and volumetric activities of the immobilized enzyme samples with indole (2.5 mM) and NADPH (0.25 mM) at 30 $^{\circ}$ C and pH 7.0 were then measured with 40 μ L of the immobilization mixtures in 200 µL reactions (5-fold dilution) to obtain the final enzyme concentrations shown. The formation of indigo and consumption of NADPH were spectrophotometrically monitored. Control reactions were performed without scaffolds. At P450 enzyme concentrations >0.8 µM, NADPH was consumed after 30 s, preventing reliable activity measurements. The same experiments were performed with unmodified His-P450BM3m as a control (see Figure S17). (d) Influence of different scaffolds on P450BM3m and PTDH activities was determined by immobilizing P450BM3m (8

Figure 7. continued

 μ M) or PTDH (0.5 μ M) as in (b) prior to activity measurements. Control reactions were performed without scaffolds and enzymes without SpyT and SnoopT fusions. Specific activities for P450BM3m were measured with indole as in (c) by monitoring indole formation. Specific activities for PTDH were measured with sodium phosphite (1 mM) and NADP+ (0.25 mM) by monitoring NADPH formation. Reactions were performed with 40 μ L immobilization samples in 200 μ L assays at 30 °C and pH 7.0. Using the same setup, stability of the immobilized enzymes was determined by measuring specific activities immediately and after up to 168 h (30 °C, pH 7.0) after mixing of enzymes and scaffolds (Figures S18 and S19). For (b,c), detailed protocols with protein concentrations are provided in the Methods. For (c,d), data are shown as mean values \pm SD and error bars represent the standard deviations of four replicates with one set of purified proteins.

Table 1. P450BM3m Kinetic Parameters

enzyme	$K_{_{ m m}} \; (\mu m M)$	$k_{\rm cat}~({\rm s}^{-1})$	$k_{\rm cat}/K_{\rm m}~({ m M}^{-1}~{ m s}^{-1})$	Hill coefficient
		indole ^a		
His-P450BM3m	631.8 ± 46.8	0.1 ± 0.01	2.3×10^{2}	2.7 ± 0.3
His-SpyT-P450BM3m-SnoopT	691.3 ± 18.3	0.2 ± 0.003	2.8×10^{2}	2.0 ± 0.1
		indole ^b		
His-P450BM3m	179.3 ± 22.2	0.6 ± 0.03	3.3×10^{3}	1.6 ± 0.2
His-SpyT-P450BM3m-SnoopT	302.1 ± 27.8	0.8 ± 0.03	2.6×10^{3}	1.3 ± 0.1
		NADPH ^a		
His-P450BM3m	70.7 ± 2.3	0.1 ± 0.01	2.1×10^{3}	7.0 ± 1.2
His-SpyT-P450BM3m-SnoopT	74.4 ± 0.8	0.2 ± 0.004	2.4×10^{3}	6.6 ± 0.2
		lauric acid ^b		
His-P450BM3m	121.1 ± 14	2.2 ± 0.1	1.8×10^{4}	1.5 ± 0.3
His-SpyT-P450BM3m-SnoopT	95.8 ± 6.2	2.5 ± 0.1	2.6×10^{4}	1.8 ± 0.3

^aCalculated by measuring indigo formation at 670 nm. ^bCalculated by measuring NADPH oxidation at 340 nm. *Enzyme reactions were performed at 30 °C in sodium phosphate buffer (pH 7.0) with 0.4 μM His-tagged wild-type dual-modified P450BM3m (see Methods). The His-SnoopC-P450BM3m-SpyC fusion protein was inactive, and no kinetic parameters could be measured. Data are shown as mean values ±SD and error bars represent the standard deviations of four replicates with one set of purified proteins. Kinetic fitting curves are shown in Figure S15.

Table 2. PTDH Kinetic Parameters^a

enzyme	$K_{ m m}~(\mu{ m M})$	$k_{\rm cat}~({\rm s}^{-1})$	$k_{\rm cat}/K_{\rm m}~({ m M}^{-1}~{ m s}^{-1})$
	NADP ⁺		
His-PTDH	9.5 ± 1.1	2 ± 0.1	2.1×10^{5}
His-SpyT-PTDH-SnoopT	6.5 ± 0.4	1.5 ± 0.02	2.3×10^{5}
His-SnoopC-PTDH-SpyC	5.2 ± 0.9	0.1 ± 0.001	1.2×10^4
	Na ₂ HPO ₃		
His-PTDH	69 ± 2.1	2.1 ± 0.01	3.1×10^{4}
His-SpyT-PTDH-SnoopT	56.9 ± 5.9	1.5 ± 0.03	2.7×10^{4}
His-SnoopC-PTDH-SpyC	33.9 ± 4.9	0.1 ± 0.003	2.3×10^{3}

[&]quot;Enzyme reactions were performed at 30 °C in sodium phosphate buffer (pH 7.0) with 0.03–0.25 μ M PTDH (see Methods). Data are shown as mean values \pm SD and error bars represent the standard deviations of four replicates with one set of purified proteins.

including indole into the blue indigo for convenient activity assessment. 44-46 For cofactor recycling and the operation of a two-enzyme cascade on scaffolds (Figure 7a), we selected an engineered PTDH that is known to work with P450BM3. 19,41,47,48 For scaffold conjugation and cross-linking, the N and C termini of P450BM3m and PTDH were modified with Spy/Snoop-Catcher and -Tag fusions. While comparing the kinetic properties of the enzymes (Tables 1 and 2), we found that fusion of the larger Catcher domains (9.1 kDa SpyC and 12.6 kDa SnoopC) completely inactivated P450BM3m and reduced the activity of PTDH more than 10-fold. The addition of the smaller Spy/Snoop-Tag did not significantly impact enzyme activities and thus yielded active enzymes for conjugation to SpyC-EutM-SnoopC-modified scaffolds. Under the reaction conditions tested (0.1 M sodium phosphate buffer, pH 7.0, 30 °C), P450BM3m exhibited non-Michaelis-Menten, sigmoidal kinetics (Figure S15), which has been reported for P450BM3 with non-natural substrates like indole and different buffer conditions. $^{46,49-53}$ This sigmoidal behavior was more pronounced when measuring steady-state kinetics

with varying concentrations of NADPH (5 mM indole) as indicated by a more than 3-fold higher Hill coefficient (2.0 vs 6.6 for His-SpyT-P450BM3m-SnoopT) (Table 1), suggesting homotropic cooperativity and/or NADPH uncoupling. Each enzyme (His-SpyT-P450BM3m-SnoopT and His-SpyT-PTDH-SnoopT and controls His-P450Bm3m and His-PTDH) was then individually conjugated His-SpyC-EutM-SnoopC and hybrid His-EutM:SpyC-EutM-SnoopC scaffolds at a 1:4 molar ratio to the dual-modified EutM building block. At this molar ratio, we obtained efficient conjugation of GFP cargo and expected to achieve sufficient spacing of the immobilized catalysts, 14 especially considering the large size of P450BM3m (248 kDa for the dimer). Both enzymes were efficiently cross-linked individually as well as together to scaffolds and formed higher molecular weight complexes as observed with the GFP cargo (Figures 7b and S16). Because P450BM3m is a highly dynamic protein that associates as a functional dimer,⁵⁴ we determined its specific and volumetric activities at different enzyme concentrations for indigo formation and NADPH consumption when conjugated at

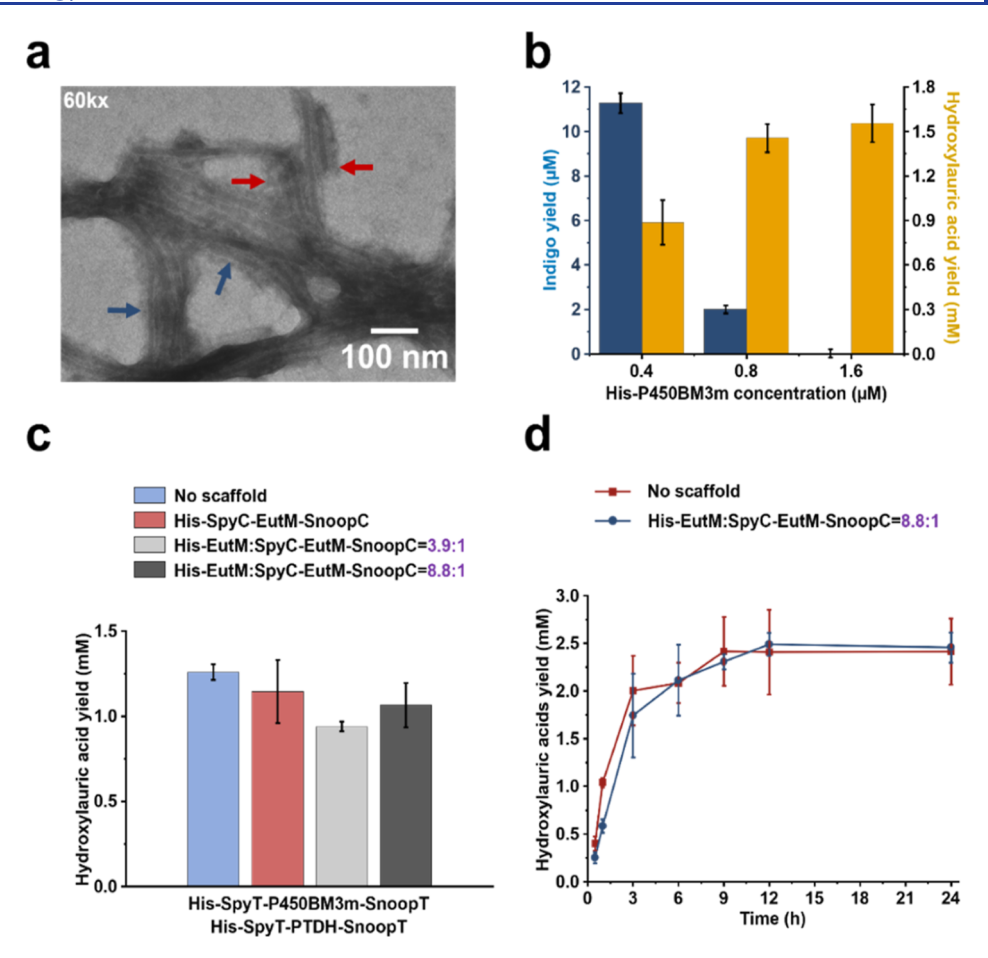


Figure 8. Coimmobilization of P450BM3m and PTDH onto hybrid scaffolds. (a) TEM of His-EutM:SpyC-EutM-SnoopC = 8.8:1 hybrid scaffolds with coimmobilized P450BM3m and PTDH shows cross-linked tube-like structures enveloped in a dense coating as in Figure 6a with GFP. Samples were prepared by coimmobilizing 15 μ M of each enzyme with 120 μ M His-EutM:SpyC-EutM-SnoopC = 8.8:1 as in Figure 7b. Samples were diluted (1 mg/mL) prior to TEM. Additional images and magnifications (10k-120k×) are provided in Figure S20. (b) Testing of the coupled reaction system with free His-PTDH and His-P450BM3m. For indole conversion (blue), reactions were performed at 30 °C and pH 7.0 in 0.1 M phosphate buffer with 1.6 μ M His-PTDH and 0.4, 0.8, or 1.6 μ M His-P450BM3m and 2.5 mM indole, 10 mM sodium phosphite, and 0.25 mM NADP*. After 15 min, indigo was spectrophotometrically quantified. For lauric acid conversion (gold), reactions were performed under the same conditions and concentrations but with 2.5 mM lauric acid. Reactions were stopped after 15 min and hydroxylauric acids (combined 9-, 10-, and 11-hydroxylauric acids, see Figures S24 and S25) were quantified by a gas chromatography-flame ionization detector (GC-FID). (c) Demonstration of coupled reaction with P450BM3m and PTDH coimmobilized onto scaffolds. Dual-modified P450BM3m and PTDH (6.4 µM each) were coimmobilized onto scaffolds (or no scaffolds as a control) at a 1:4 molar ratio of enzymes to the cross-linking scaffold building block in the scaffolds as in Figure 7d. 1 mL of lauric acid conversion reactions was then performed for 10 min with 500 µL of enzyme mixture (3.2 µM final enzyme concentrations) with the conditions in (b). Relative amounts of hydroxy lauric acid conversion products for the reactions are shown in Table S2. (d) Two-phase reaction system for lauric acid conversion. A 5 mL reaction was set up with 2.5 mL immobilized enzyme mixtures as in (c) but with 0.8 μ M His-SpyT-P450BM3m-SnoopT, 3.2 μ M His-SpyT-PTDH-SnoopT, 50 mM sodium phosphite, 0.5 mM NADP⁺, and 20 mM lauric acid in 20% (v/v) dodecane. Reactions were performed at 30 °C, 120 rpm and hydroxylauric acid products quantified. Detailed protocols with protein concentrations for scaffolds and enzymes are provided in the Methods. Data in (b-d) are shown as mean values $\pm SD$ and error bars represent the standard deviations of four replicates with one set of purified proteins.

either terminus to His-SpyC-EutM-SnoopC scaffolds (1:4 molar ratio of the enzyme to scaffold building block) (Figure 7c). The highest volumetric activity for indigo formation was achieved with 1.6 μ M dual-modified P450BM3m attached to the scaffolds. Scaffold attachment also benefited NADPH oxidation activity. Interestingly, control reactions with unmodified P450BM3m show a similar trend, suggesting that the scaffolds by themselves without cross-linking provide a beneficial reaction environment presumably through interactions between enzymes and scaffold proteins (Figure S17).

Next, we compared specific activities of P450BM3m and PTDH immobilized to different scaffolds (1:4 molar ratio of the enzyme to the conjugating scaffold building block). Control reactions were performed with no scaffolds and

unmodified enzymes. The final reactions were performed with the optimal P450BM3m concentration of 1.6 μ M (which gave the highest volumetric activity, Figure 7c) or with 0.1 μ M of the much more active PTDH (Tables 1 and 2). As observed before, scaffolds did not reduce enzyme activities, and crosslinking slightly increased specific activities of P450BM3m or PTDH (Figures 7d, S18, and S19). Scaffold type did not significantly affect the enzymes' specific activities, except that activities with His-EutM:SpyC-EutM-SnoopC = 8.8:1 hybrid scaffolds were slightly lower. Due to the high turbidity of these macroscale scaffolds that also adsorbed some of the formed indigo (yielding blue scaffold material), P450 activity measurements were challenging, resulting in large standard deviations.

Finally, enzyme stability was measured by incubating the scaffolded and unscaffolded enzymes and controls under the above conditions (pH 7.0, 30 $^{\circ}$ C) and concentrations (8 μ M P450BM3m or 0.5 μ M PTDH conjugated at a 1:4 molar ratio of the enzyme to conjugating scaffold building block) for up to 168 h (7 days) prior to activity measurements with 5-fold diluted samples containing 1.6 μ M P450BM3m or 0.1 μ M PTDH (Figures S18 and S19). Under these incubation conditions, P450BM3m was remarkably stable with little loss of activity. PTDH was less stable with the unmodified and dual-modified enzymes retaining 50% and 35%, respectively, of their activities after 7 days. In the presence of scaffolds, the stabilities of the enzymes increased about 15%. Interestingly, only the hybrid scaffolds increased dual-modified PTDH stability, while scaffold protein addition regardless of type stabilized the unmodified PTDH, suggesting that surface attachment and the resulting different electrostatic environments matter for enzyme stability.

In summary, these results demonstrated that the designed scaffolding system functions as an effective enzyme immobilization platform that is even compatible with a large, multidomain enzyme like P450BM3m. In addition, the scaffolds can stabilize less stable enzymes as we have observed before. ^{14,16}

Coimmobilization of P450BM3m and PTDH Operation of Two-Enzyme Reaction. As a final test, we coimmobilized P450BM3m and PTDH onto our scaffolds for cofactor recycling and to demonstrate catalysis with more than one enzyme (Figure 7a). P450BM3m and PTDH are efficiently coimmobilized to hybrid His-EutM:SpyC-EutM-SnoopC = 8.8:1 scaffolds, forming large molecular weight complexes similar to those observed with the conjugated, individual enzymes (Figure 7b). Negative staining TEM of diluted hybrid scaffolds (Figures 8a and S20) with the coimmobilized enzymes shows parallel aligned tubes that are enveloped by a thick film, indicating successful coating and cross-linking of scaffolds with the two cargo enzymes as observed with GFP (Figures 6a and S14).

During optimization of the coupled reaction of P450BM3m and PTDH with the free enzymes for NADPH recycling with indole as the substrate, we unexpectedly found that at higher P450BM3m concentrations (including the optimal scaffold immobilization concentration of 1.6 μ M determined in Figure 7c for the highest volumetric activity) and 0.25 mM NADPH, indigo production was either completely abolished or greatly inhibited in the coupled system compared to P450BM3m-only reactions with 0.25 mM NADPH (Figures 8b and S21). We suspected that this inhibition may be caused by the production of inactivating oxygen species and/or H₂O₂ ^{38,55,56} because of the uncoupling of NADPH electron transfer with the nonnative indole as the substrate due to the maintenance of a high NADPH concentration by the cofactor recycling PTDH. The inhibition of indole conversion can be replicated with the unmodified and dual-modified His-P450BM3m enzymes in reactions with both high NADPH (3.5 mM) and P450BM3m (1.6 μ M) concentrations (Figure S21). We tested the same coupled P450BM3m and PTDH reaction system with lauric acid as the natural substrate of P450BM3. The catalytic efficiency of P450BM3m with lauric acid was 2 orders of magnitude higher compared to indole (Table 1). In addition, the NADPH coupling efficiency of P450BM3m for lauric acid was determined to be at least 10-fold higher than for indole $(54.0 \pm 17.8\% \text{ compared to } 3.3 \pm 0.5\%, \text{ see Methods})$. No

inhibitory effect on lauric acid hydroxylation was observed at higher P450 enzyme concentrations in the coupled reaction system with the free enzymes (Figure 8b). We therefore proceeded to evaluate scaffold coimmobilization of our model two-enzyme system with lauric acid to minimize uncoupling effects upon immobilization.

After testing different P450BM3m and PTDH concentrations (Figure S22), we coimmobilized P450BM3m and PTDH at a 1:1 ratio (final enzyme concentrations in the reaction: 3.2 µM each) onto scaffolds. Conjugation to His-SpyC-EutM-SnoopC and His-EutM:SpyC-EutM-SnoopC = 3.9:1 or = 8.8:1 scaffolds decreased hydroxylauric acid yields 10%, 25%, and 15%, respectively, compared to the free enzyme system, which is comparable to the reduction of lauric acid activity obtained for carrier-immobilized P450BM3³⁸ (Figure 8c). Scaffold conjugation did not affect hydroxylation site selectivity of P450BM3m with 9-hydroxylauric acid being the major product followed by 10- and 11-hydroxylauric acid (Table S2). The lower product yields of the scaffolded reaction systems may be due to minor diffusion limitations of the substrate in the cross-linked scaffold material but more likely also to higher electron uncoupling when the two enzymes are colocalized in proximity and thus exposure of P450BM3m to high local NADPH concentrations.

To test recycling and reuse of the scaffolds, we repeated this reaction and scaled up to 3 mL with the P450BM3m and PTDH coimmobilized onto the His-EutM:SpyC-EutM-SnoopC = 8.8:1 hybrid scaffolds (Figure S23) for four cycles. After each 30 min of reaction, the scaffolded enzymes were recovered by centrifugation and reused in the next reaction cycle. Hydroxylauric acid yields and protein recovery after each reaction cycle were measured for comparison. While the P450BM3m lost over 60% of its activity after the first reaction cycle and with almost all the enzyme inactivated after three cycles, the hybrid scaffold material proved to be remarkably robust, with ~82% of the protein material recovered after 4 cycles despite the use of a relatively low protein concentration (4.4 mg/mL) in the reaction mix.

Finally, we tested a two-phase reaction system with 20% (v/ v) dodecane, 2% DMSO, and 20 mM lauric acid (soluble up to 2 mM in water)⁴⁶ for lauric acid conversion with a 4-fold decreased P450BM3m concentration to slow conversion time and allow for longer time course measurements (Figure 8d). Compared to the soluble enzyme system, scaffold immobilization did not benefit initial lauric acid conversion and had only a small effect on the total turnover number (TTN) of the scaffolded P450BM3m which was 3110.7 ± 148.0 compared to a TTN of 3009.9 \pm 554.1 for the free enzyme after 12 h of reaction when maximal conversion is reached. The time course of the conversions shows that like in the reuse experiment (Figure S23), P450BM3m is rapidly inactivated (even at the reduced enzyme loading), presumably due to the production of H₂O₂. This together with a slow mass transfer of lauric acid from the dodecane phase in the biphasic reaction 46 results in only a ~12% conversion of lauric acid.

In summary, to increase conversion yields and TTN, additional optimization efforts such as fine-tuning enzyme activities, optimizing the reaction system for substrate delivery, use of wild-type P450BM3, catalase incorporation, ³⁸ or separate immobilization of P450BM3m and its NADPH recycling system ⁴⁰ will be required to mitigate P450 inactivation that are beyond the scope of this work. For demonstration purposes, the genetically programable protein-

based scaffolding system compares favorably with other more mature biocatalyst immobilization methods. ^{38,39,41,57,58} It allows for the cross-linking of a challenging and complex enzyme without any significant reduction in activity. Furthermore, the macroscale protein carrier material does not appear to significantly impede substrate diffusion, probably due to its assembly into scaffold structures composed of radial microtube bundles with large surface areas for enzyme conjugation and cross-linking.

CONCLUSIONS

We successfully developed a programmable protein scaffold with two controllable conjugation sites for cargo attachment and cross-linking using the isopeptide bond forming a Spy/Snoop-Catcher and -Tag system. By controlling the coexpression levels of unmodified and with conjugation-site-modified EutM, we were able to readily produce macroscale protein materials with different building block ratios for customizable functionalization.

We observed that higher levels of unmodified EutM or EutM modified at the N and C termini with the smaller Spy/Snoop-Tags promoted self-assembly into larger and denser scaffold materials composed of microtubular, radial structures. Although the Spy/Snoop-Catcher dual-modified EutM building blocks assemble into smaller, soluble scaffolds, coexpression with unmodified EutM building blocks drives the assembly of large, insoluble hybrid scaffolds that are stable under a range of conditions. Instead of sheet-like structures, the scaffolds form hollow, rolled-up microtubes that increase in diameter and thickness when hybrid scaffolds are coassembled from His-EutM and SnoopT-EutM-SpyT. These microtubes organize into clusters of radial scaffold particles with large surface areas to which tagged cargo proteins can be rapidly attached, coating surfaces and cross-linking tubes into larger bundles.

We furthermore demonstrated that our designed materials are well-suited for enzyme immobilization, supporting covalent attachment of a complex P450 enzyme without loss of activity and change of the product profile despite immobilization at either end of the enzyme. Coimmobilization of two enzymes is also readily achieved, but for our P450BM3m model system, coimmobilization of PTDH exacerbated rapid P450 inactivation, presumably due to high local NADPH concentrations produced by PTDH, leading to creation of reactive uncoupling products. While this challenge may be overcome by additional optimization of the system, this is outside the scope of this work. Nevertheless, the recycling experiments demonstrated that the designed protein scaffolds yield robust, macroscale materials that can be recovered from reactions with >80% yield after several rounds of centrifugation even when used at low protein concentrations—which is an important property for future applications in heterogeneous reaction systems.

We observed that the genetic fusion of the larger Spy/Snoop-Catcher domains to cargo enzymes negatively affected the enzyme function. Our scaffolding system can be easily adapted to not only allow for the inclusion of alternative genetically encoded protein—protein interaction mechanisms for attachment but also separate cross-linking from attachment of enzymes or other proteins.

Numerous native or designed proteins can be envisioned to be utilized as cross-linkers to control material properties, while the attachment of enzyme or other proteins will yield functional materials, for example, for biomanufacturing, as

functional coatings or conducting and sensing materials. For biocatalytic applications, our genetically engineered materials enable specific and precise enzyme attachments via genetically fused tags as opposed to the unspecific and often multipoint (impeding enzyme activity) attachments of traditional immobilization systems. This work serves as a first step toward using scaffold building blocks and different conjugation tags for the design of materials with which to control enzyme loading and spatial organization. By taking advantage of the natural diversity as well as engineerability of our scaffold building blocks, future scaffolds could present surface properties optimized to support individual enzyme functions and provide operational benefits, e.g., for cofactor, substrate, or product mobilization. Future efforts should also be directed toward the design of a programmable switch with which to better control the assembly of hexamers into soluble or insoluble, macroscale scaffolds, which would allow one-step functional material production and recovery as a major cost reduction step for future process scale-up as well as improved control over material composition and structures, potentially reducing scaffold heterogeneity. Future incorporation of different genetically encoded cross-linkers independent of cargo proteins and enzymes will add yet another dimension to the programmability of our platform.

In summary, together with the prospect of eventually programming the fabrication of the entire material in a recombinant cell-based or, in the future, cell-free system, our robust scaffolding system provides a highly adaptable and customizable platform for the design of a multitude of functional materials.

METHODS

Materials and Chemicals. All chemical reagents were purchased from Sigma-Aldrich (St. Louis, MO, USA) unless otherwise noted. Lauric acid (≥99.0% GC, catalog #61610), palmitic acid (≥98.5%, catalog #76120), and 12-hydroxylauric acid (≥97%, catalog #55499) were obtained from Honeywell Fluka (Morris Plain, NJ, USA). Except for the PCRBIO VeriFi Mix from Genesee Scientific (Morrisville, NC, USA) used for colony PCR, all other molecular biology reagents (HiFi DNA Assembly Master Mix for Gibson assembly and other enzymes) were obtained from New England Biolabs (Ipswich, MA, USA). Oligonucleotides were purchased from Integrated DNA Technologies, Inc. (Coralville, IA, USA).

For purification and PAGE analysis of proteins, Spectra/Por Dialysis Tubing (MWCO 6-8 kDa) from Spectrum Life Sciences (Rancho Dominguez, CA, USA) was used for dialysis, and HisPur Ni-NTA resin from Thermo Fisher Scientific (Waltham, MA, USA) was used for metal affinity chromatography. For P450BM3m purification, Roche cOmplete Protease Inhibitor Cocktail tablets purchased from Sigma-Aldrich were used. The Pierce BCA Protein Assay Kit from Thermo Fisher was used to quantify protein concentrations. Except for Coomassie brilliant blue from Sigma-Aldrich, all other reagents for PAGE (TEMED, Precision Plus Protein prestained protein standard (catalog #161-0373), and 30% acrylamide and bisacrylamide solution (37.5:1)) were obtained from Bio-Rad (Hercules, CA, USA). A Milli-Q water purification system (MilliporeSigma, Burlington, MA, USA) was used to filter deionized water to prepare ultrapure water with a final electrical resistance higher than 18.2 M Ω cm⁻¹.

Bacterial Strains, Media, and General Cloning Methods. Cloning and plasmid propagation were done in *E*.

coli TOP10 (Invitrogen, Carlsbad, CA, USA), while *E. coli* BL21 (DE3) (New England Biolabs, Ipswich, MA, USA) was used for expression of proteins for purification. *E. coli* strains were grown in Luria broth (LB; tryptone 10 g/L, NaCl 5 g/L, yeast extract 10 g/L) medium supplemented with appropriate antibiotics [100 μ g/mL ampicillin (LB-Amp) or 30 μ g/mL kanamycin (LB-Km)] for plasmid maintenance. For cytochrome P450BM3m protein expression and purification, LB medium was replaced with Hyper Broth (AthenaES, Baltimore, MD, USA).

Plasmid transformation into *E. coli* followed standard molecular biology techniques. Transformants were confirmed by colony PCR and all gene and plasmid sequences were verified by Sanger sequencing (ACGT Inc., Wheeling, IL, USA) and complete plasmid Nanopore sequencing (Plasmidsaurus, Eugene, OR, USA).

Plasmid Construction. Plasmids were constructed using a combination of methods, including Gibson Assembly (HiFi DNA assembly kit from New England Biolabs), T5 exonuclease-dependent assembly for fragment assembly, and site-directed mutagenesis (Q5 kit, New England Biolabs) for short insertions, deletions, and mutations as described previously. 14,33

For amplification and cloning of His-tagged GFP cargo and EutM with and without SpyTag/SpyCatcher fusions, we used previously described plasmids as templates and backbones (pCT5BB or pET28a).14 The PTDH nucleotide sequence and SnoopCatcher sequence were synthesized by Genewiz (South Plainfield, NJ. USA). The wild-type P450BM3 gene was amplified from genomic DNA isolated from Bacillus megaterium^{3,44} and three amino acid substitutions (Ala74Gly, Phe87Val, and Leu188Gln) were introduced into the cloned gene by site-directed mutagenesis to yield the indigoproducing variant P450BM3m.44 Shorter Snoop/SpyTag and GS-linker sequences and RBSs were inserted by site-directed mutagenesis. All plasmids used and constructed are listed in Table S3. Amino acid sequences and encoding nucleotide sequences for EutM scaffolds, GFP cargo proteins, and enzymes are provided in Tables S4 and S5.

Briefly, cargo protein cloning started with the assembly of GFP into the NdeI site of pET28a, followed by the insertion of Spy/Snoop Tag/Catcher fusions and GS-linkers up- and downstream of GFP. GFP was replaced by PTDH or P450BM3m to yield the corresponding cargo protein expression plasmids. Plasmids for EutM scaffold protein expression were constructed using pCT5BB-His-EutM14,16 as a template to create pCT5BB-His-SnoopT-EutM-SpyT and pCT5BB-His-SpyC-EutM-SnoopC plasmids for the expression of dual-modified EutM proteins. Hybrid scaffold expression plasmids were constructed by amplifying His-EutM from pCT5BB-His-EutM along with its upstream RBS (strong native RBS in pCT5BB referred to as RBSA) and inserting it upstream of the RBSA site of the dual-modified EutM expression cassettes. Site-directed mutagenesis was used to change the His tags and delete the RBSs. RBSs with different strengths in addition to the native RBSA from pCT5BB were selected based on previous work³² and predictions using the online RBS calculator developed by the Salis group (https:// salislab.net/software/predict rbs calculator) (Table S1).

Protein Expression in *E. coli***.** For the expression of EutM scaffolds from the cumate-inducible promoter on pCT5BB plasmids, single colonies of *E. coli* BL21 (DE3) transformants were inoculated into 50 mL of LB-Amp and grown overnight

(30 °C, 180 rpm). Overnight cultures were diluted 100-fold into fresh LB-Amp (200 mL in 1 L flasks or 400 mL in 2 L flasks) and grown at 37 °C and 180 rpm until OD₆₀₀ = 0.6–1.0 when protein expression was induced with 50 μ M cumate. Induced cultures were grown for 16–20 h at 37 °C, 180 rpm, and cells were harvested by centrifugation at 4000g for 25 min at 4 °C. Cell pellets were stored at -80 °C until needed.

For the expression of GFP cargo proteins from the T7 promoter on pET28a plasmids, LB-Amp was replaced with LB-Km and protein expression and cell harvest followed the same procedure except that protein expression was induced with 0.1 mM isopropyl β -D-1-thiogalactopyranoside (IPTG). For PTDH cargo protein expression from the T7 promoter on a pET28a plasmid, the temperature of the overnight culture was lowered to 25 °C prior to induction, and the induced cultures were grown for 16–20 h at 180 rpm until harvest of cell pellets which were stored at $-80~^{\circ}\text{C}$ until needed.

For cytochrome P450BM3m cargo protein expression from the T7 promoter on pET28a plasmids, *E. coli* BL21(DE3) transformants were grown overnight in 50 mL of LB-Km (30 °C, 180 rpm). Overnight cultures were diluted 1:20 into Hyper Broth (AthenaES, catalog #0107, 400 mL in 2 L flasks) supplemented with 30 μ g/mL kanamycin, 1 mM MgSO₄, 0.1 mM FeCl₂, and 1× trace elements⁶⁰ and grown (37 °C, 180 rpm) until OD₆₀₀ = 1.0–1.5 (~3–4 h). Cultures were cooled in an ice—water bath for 20 min and then induced with 0.1 mM IPTG. To ensure sufficient heme biosynthesis, δ -aminolevulinic acid was added (1 mM final concentration) at this time. Induced cultures were grown at 22 °C and 140 rpm for 16–20 h until harvest and storage as described above.

EutM Scaffold and GFP Cargo Protein Purification. For the purification of the soluble dual-modified EutM scaffolds and GFP cargo proteins, E. coli cells were suspended in lysis buffer without urea (20 mM imidazole, 50 mM Tris-HCl, 250 mM NaCl, pH 8.0) and disrupted by sonication (30 min, power 40%, pulse on 1 s, and pulse off 2 s on ice with a Branson Sonifier). The lysed cells were centrifuged (10,000g, 30 min, 4 °C) and the His-tagged proteins in the supernatant purified using the Batch Protocol with the HisPur Ni-NTA resin according to the manufacturer's instructions (Thermo Fisher). Briefly, the clarified supernatant was mixed with resin and incubated for 1 h at 4 °C. The mixture was then loaded onto a gravity-flow column and washed with lysis buffer, and bound proteins eluted with five resin-bed volumes of elution buffer (250 mM imidazole, 50 mM Tris-HCl, 250 mM NaCl, pH 8.0).

For the purification of wild-type, hybrid-EutM scaffolds, samples for assembly testing, and native PAGE analysis of dual-modified EutM scaffolds (Figures S2 and S4), 4 M urea was added to both lysis and elution buffers to disassemble and solubilize large EutM scaffolds. The purified, eluted proteins were then concentrated with an Amicon Ultra Centrifugal Filter (3 kDa MWCO) to a concentration of 20–40 mg/mL if needed. To remove imidazole and/or urea, purified and concentrated proteins were dialyzed against 50 mM Tris-HCl buffer (pH 7.5) (or other buffers where indicated) at 4 °C overnight using Spectra/Por Dialysis Tubing (6–8 kDa MWCO).

PTDH and P450BM3m Cargo Enzyme Purification. E. coli cells were resuspended and lysed by sonication as described above, except that for P450BM3m purification, the cell density for lysis was controlled to 4 mL of buffer per gram of cell wet weight and 1 mg/mL lysozyme and Roche

cOmplete Protease Inhibitor was added to the buffer according to the manufacturer's instructions. Proteins were purified by Ni-NTA affinity chromatography as described above with the exception that the column was washed with a buffer (50 mM Tris-HCl, 250 mM NaCl, pH 8.0) containing 45 mM imidazole and proteins were eluted with five volumes of elution buffer. The buffer of the eluted protein samples was exchanged to a 0.1 M sodium phosphate buffer (pH 7.0) with a PD-10 desalting column (GE HealthCare, Buckinghamshire, UK). Proteins were concentrated to 40–80 mg/mL with an Amicon Ultra Centrifugal Filter (10 kDa MWCO). Concentrated proteins were then mixed 1:1 v/v with glycerol and aliquots flash-frozen in liquid nitrogen for storage at -80 °C until needed. All protein purifications were performed at least three times from fresh transformed *E. coli* strains.

Labeling of His-SpyC-EutM-SnoopC Scaffolds Bound to Beads with GFP and mCherry. A 1.6 mg portion of the His-SpyC-EutM-SnoopC scaffold was incubated with 4 μ L of HisPur Ni-NTA resin (Thermo Scientific, 0.4 mg protein/ μ L bead) in 500 μ L of 50 mM Tris-HCl pH7.5 at 30 °C for 1 h. Samples were then mixed with 10 μ g/mL of unmodified His-GFP and His-mCherry as controls or GFP-SpyT-His and His-SnoopT-mCherry, individually or in combination. After 1 h incubation at 30 °C, beads were washed once with 1 mL of 50 mM Tris-HCl pH7.5 and resuspended in 50 μ L of this buffer for observation of GFP and mCherry labeling by fluorescence microscopy (see below).

SDS-PAGE and Protein Concentration Analysis. Purity and protein sample compositions of scaffolds, cargo proteins, and enzymes were analyzed by 15% SDS-PAGE following standard methods with samples diluted 6× with loading buffer and denatured for 20 min at 100 °C prior to loading. Protein concentrations were measured with the Pierce BCA assay kit using the manufacturer's 60 °C protocol.

Native PAGE Analysis of EutM Scaffolds. Purified EutM scaffold proteins were normalized to 2 mg/mL with elution buffer containing 4 M urea and then mixed with 2× native PAGE sample buffer (62.5 mM Tris-HCl, 40% glycerol, 0.01% bromophenol blue, pH 6.8), separated on 4–15% Mini-PROTEAN TGX Stain-Free Protein Gels (Bio-Rad catalog #4568083), and stained with Bio-Safe Coomassie Stain (Bio-Rad catalog #1610786) (Figure S2)

GFP Cargo-Cross-Linking to Different EutM Scaffolds. Purified GFP cargo proteins (dual-modified and unmodified control) and EutM scaffold or hybrid scaffold proteins [20-40 mg/mL in 0.1 M sodium phosphate buffer (pH 7.0)] were mixed with the isopeptide bond-forming partners (e.g., 50 μ M His-SpyT-GFP-SnoopT with 50 μM His-SpyC-EutM-SnoopC scaffold or with 50 μ M SpyC-EutM-SnoopC in the His-EutM:SpyC-EutM-SnoopC scaffold). Reactions were performed in a 0.1 M sodium phosphate buffer (pH 7.0) (200 μ L final volume) prior to mixing with sample buffer for SDS-PAGE analysis (Figures 2b and S10) or for imaging by microscopy or TEM (Figures 5, 6, and S14). To characterize cargo cross-linking under different conditions, reactions were performed with a 1:1 molar ratio of 50 μ M cross-linking partner proteins under different conditions, including 1 h at different temperatures (4, 25, 30, and 37 °C) and 25 °C for up to 24 h with samples taken at different intervals (Figure S3). In addition, reactions were performed with different molar ratios of partner proteins by mixing 50 µM EutM scaffold partner with 12.5, 25, 50, 100, and 200 μ M GFP cargo protein for 1 h

at 25 $^{\circ}$ C and 180 rpm prior to analysis by microscopy (Figures S11 and S13).

The final scaffold and GFP cargo protein concentrations in the samples for these reactions were (i) for 50 μ M EutM scaffolds: 1.7 mg/mL for His-SpyC-EutM-SnoopC (34.3 kDa) (w/o His-Tag in hybrid scaffolds = 32.7 kDa, 1.6 mg/mL) and 0.8 mg/mL for His-SnoopT-EutM-SpyT (15.8 kDa) (w/o His-Tag in hybrid scaffolds = 14.5 kDa, \sim 0.7 mg/mL); (ii) for 50 μM of dual-modified EutM in the hybrid scaffold designs containing different ratios of His-EutM (11.5 kDa, 50 μ M = 0.6 mg/mL): 3.9 mg/mL His-EutM:SpyC-EutM-SnoopC = 3.9:1, 6.7 mg/mL His-EutM:SpyC-EutM-SnoopC = 8.8:1, 2.6 mg/mL His-EutM:SnoopT-EutM-SpyT = 3.3:1, and 5.1 mg/ mL His-EutM:SnoopT-EutM-SpyT = 7.6:1; and (iii) for the different concentrations of the GFP cargo protein: 0.7, 1.3, 2.6, 5.2, and 10.4 mg/mL corresponding to 12.5, 25, 50, 100, and 200 μ M His-SnoopC-GFP-SpyC, 0.4, 0.8, 1.7, 3.3, and 6.6 mg/ mL corresponding to 12.5, 25, 50, 100, and 200 μM His-SnoopT-GFP-SpyT, and 1.5 mg/mL corresponding to 50 μ M His-GFP.

In Vitro Scaffold Coassembly of EutM Scaffold Building Blocks. To investigate in vitro coassembly of purified EutM scaffold building blocks into hybrid scaffolds, purified scaffold building blocks (2 mg/mL) in elution buffer with urea were mixed at a 5:1 molar ratio (His-EutM:dualmodified EutM) and dialyzed against a 50 mM Tris-HCl buffer (pH 7.5). The assembled scaffolds were then analyzed by native PAGE and compared to controls with single building blocks (Figure S2). The same samples were also analyzed by SDS-PAGE after separating soluble (S) and insoluble scaffolds as pellet (P) by centrifugation at 12,000g for 2 min (Figure S4).

Hybrid Scaffold Characterization. The total yield of hybrid EutM scaffolds from 200 mL cultures was determined by measuring the protein concentration in the eluted, purified protein fraction (5 mL) after metal affinity chromatography. Expression, purification, and subsequent characterization experiments were performed with samples obtained from three different cultures for each genetic construct. The EutM scaffold building block ratios in the different hybrid scaffolds were determined by measuring protein concentrations of EutM proteins by densitometry of SDS-PAGE gels with a standard curve of 0.1–1.0 mg/mL of purified His-EutM. Quantification was performed using the ImageJ (version 1.530) software following the protocol described by the Starr Lab and originally written by Luke Miller⁶¹ (Figures 3b and S5). Representative SDS-PAGE gels are shown in Figure S6.

To assess scaffold assembly behavior, purified hybrid scaffolds in elution buffer with urea were normalized to 2 mg/mL with elution buffer and then dialyzed against 50 mM Tris-HCl buffer (pH 7.5) at 4 °C overnight using Spectra/Por Dialysis Tubing (6–8 kDa MWCO). During dialysis, insoluble, larger scaffolds assembled, resulting in the formation of a white protein material. These insoluble scaffolds (pellet) were separated from soluble scaffolds by centrifugation at 12,000g for 2 min at room temperature. The protein concentration of the soluble fraction (S) and the insoluble scaffolds (P, pellet) after resuspension in 50 mM Tris-HCl buffer (pH 7.5) was measured to calculate the percentage of insoluble assembled scaffolds of the total scaffold protein concentration as P/P in % (Figures 3b and S5).

To investigate the influence of pH, temperature, and NaCl concentrations on scaffold assembly, purified hybrid scaffolds

in elution buffer were normalized to 3 mg/mL with elution buffer and first dialyzed as described above into the following buffers: 0.1 M sodium acetate (pH 5), 0.1 M sodium phosphate (pH 6, pH 7, or pH 7.5), and 0.1 M Tris-HCl (pH 7.5, pH 8, or pH 9). The buffer-exchanged scaffolds were then normalized to 2 mg/mL with the same buffers without and with NaCl to achieve final concentrations of 0, 100, or 250 mM NaCl. Samples were then aliquoted and incubated for 24 h at 4, 25, 30, and 37 °C. Scaffold assembly behavior was then measured as described above to quantify the percentage of insoluble scaffold protein in the samples (Figures 4, S8, and S9).

Phase Contrast and Fluorescence Light Microscopy. For imaging cargo loading onto EutM scaffolds (Figures 5, 6b, S1, S11, and S13), $10~\mu L$ of protein sample was loaded onto a glass slide and covered with a coverslip. A Leica DM4000 microscope controlled by the Leica Application Suite X (version 3.7.4.23463) and equipped with a $100\times$ oil-immersion objective and filters for phase contrast or fluorescence imaging was used for slide examination and image capture. GFP fluorescence was visualized using a L5 fluorescence cube (BP 480/40, dichromatic mirror 505, suppression filter BP527/30) with a 1.0 s exposure time. Red fluorescence was visualized using a Y3 fluorescence cube (BP 532/26, dichromatic mirror 565, and suppression filter BP 570/70).

Confocal Fluorescence Microscopy. For imaging of 3D features of EutM scaffolds cross-linked with GFP cargo (Figure 6b), $10~\mu L$ of protein sample was applied to a glass slide and covered with a coverslip for examination with a Nikon Alplus Ti2 microscope equipped with a 60×1.42 oil lambda D objective (University of Minnesota Imaging Center). The refraction index was set to 1.51, and a GFP fluorescence cube (excitation 488 nm, emission 525 nm) with a pinhole size equal to 35.76 was used for illumination. Images were captured using a Nikon Alplus camera and Nikon's NIS Elements software (version 5.30.02). Z stacks were acquired using the microscope's ZDrive for capturing 52-55 slices with a step size of $0.1~\mu m$.

DLS Analysis. For particle size distribution analysis of hybrid EutM scaffolds (His-EutM:SpyC-EutM-SnoopC = 8.8:1) (as in Figure 5a) mixed with double-tagged GFP (and untagged GFP as a control), 100 μ L samples were analyzed using a Zetasizer Nano ZS (Malvern) (Figure S12a).

Analytical Ultracentrifugation. Sedimentation experiments were performed with a Beckman Optima AUC instrument (Minnesota Nano Center, University of Minnesota). Standard 2-channel Epon centerpieces equipped with quartz windows were filled with 460 μ L samples. After cell loading, alignment, and temperature equilibration, the samples were centrifuged using an An60-Ti rotor at 42,000 rpm and 23 °C until full sedimentation (12 h). Data were recorded by monitoring the sedimentation of the absorbance at 485 nm and finally, a total of 1500 scans were collected. All AUC data analysis was carried out using the software UltraScan3, and data editing and refinement were performed according to the protocol as described. 62 Briefly, the sedimentation velocity data were initially fitted with the two-dimensional spectrum analysis⁶³ to remove time- and radially invariant noise from the raw data and to fit the meniscus position. The sedimentation coefficient range is then estimated from an enhanced van Holde-Weischet analysis.⁶⁴

Transmission Electron Microscopy. Scaffold protein samples were diluted to 1 mg/mL in 0.1 M sodium phosphate

buffer (pH 7.0), and then, 10 μ L of samples was dropped onto a 200 mesh Formvar/Carbon grid (Electron Microscopy Sciences) and allowed to adsorb for 5 min. Fluid was removed, 10 μ L of Trump's fixative (Electron Microscopy Sciences, Hatfield, PA, catalog #11750) applied for 5 min and then removed (with filter paper), and the grid rinsed three times with ultrapure water. A drop of 1% aqueous uranyl acetate was applied to the grids and immediately removed to avoid overstaining. A JEOL-JEM1400Plus transmission electron microscope with a LaB6 tungsten filament at 60 kV was used to examine the grids. Images were captured using an Advanced Microscopy Techniques XR16 camera with an AMT Capture Engine software (version 7.0.0187) (University of Minnesota Imaging Center) (Figures 3c, 6a, 8a, S7, S14, and S20).

Image Analysis. Images were cropped, and scale bars were added using ImageJ (version 1.54f). Confocal images were analyzed using Nikon's NIS Elements AR Analysis software (version 5.42.04) for 3D reconstruction of the observed structures. The screenshot function of the analysis software was used to capture images for the slice and volume views of the reconstructed structures (Figure 6b).

Quantification of P450BM3m Concentration. Carbon monoxide (CO) difference spectrum analysis was used to determine the concentration of active P450BM3m. For this, purified P450BM3m enzyme was diluted into 0.1 M sodium phosphate buffer (pH 7.0) to a final concentration of 0.5-1 mg/mL and absorbance between 400 and 500 nm was measured with a 200 μ L sample aliquot using a Varioskan LUX Multimode microplate reader (path length = 0.58 cm) (Thermo Fisher Scientific). The P450BM3m solution was then saturated with CO (bubbling gas for 40-60 s) and reduced by the addition of few grains of sodium hydrosulfite $(Na_2S_2O_4)$. Another 200 μ L sample aliquot was taken and the absorbance was measured again between 400 and 500 nm. Functional P450BM3m concentration was calculated with this reading using the following equation: (Absorption at 450 nm - Absorption at 490 nm)/ ε x d; ε = 91 mM⁻¹ cm⁻¹ at 450 nm; $d = \text{path length.}^{19,66}$ Measurements were performed in triplicate with three separate samples.

P450BM3m Kinetic Measurements. Kinetic parameters (Table 1 and Figure S15) for P450BM3m (with and without Spy/Snoop-Tag or -Catcher fusions) were determined spectrophotometrically with a Varioskan LUX multimode microplate reader by monitoring NADPH concentrations at 340 nm ($\varepsilon = 6.22 \text{ mM}^{-1} \text{ cm}^{-1}$) with indole or lauric acid as substrates. For reactions with indole, indigo formation was also spectrophotometrically quantified at 670 nm ($\varepsilon = 3.9 \text{ mM}^{-1} \text{ cm}^{-1}$). Reactions were started by the addition of NADPH.

Assays were performed with four separate replicate samples and corresponding no-enzyme control reactions at 30 °C and 600 rpm (pulsed with 10 s on and 10 s off and low force setting) with a Varioskan LUX multimode microplate reader. Assays were carried out in 0.1 M sodium phosphate buffer (pH 7.0) with a total reaction volume of 200 μ L per sample. To determine the $k_{\rm cat}/K_{\rm m}$ for lauric acid and indole, the reactions contained 40 μ L of P450BM3m (final concentration 0.4 μ M), 2 μ L of 5–500 mM indole in DMSO (final indole concentration 0.05–5 mM) or 16 μ L of 0.625–25 mM lauric acid in DMSO (final lauric acid concentration 0.05–2 mM), and 10 μ L of 5 mM NADPH (final NADPH concentration 0.25 mM). To determine the $k_{\rm cat}/K_{\rm m}$ of the NADPH cofactor, the NADPH concentration was varied from 0.025 to 0.25 mM

NADPH (10 μ L of 0.5–5 mM NADPH) and 5 mM indole (2 μ L of 500 mM indole in DMSO) was used as the substrate. Kinetic parameters were calculated using the Hill fitting function of Origin (version 2022b).

PTDH Kinetic Measurements. Enzyme activity for PTDH (with and without Spy/Snoop-Tag or -Catcher fusions) was determined by monitoring NADPH concentrations at 340 nm $(\varepsilon = 6.22 \text{ mM}^{-1} \text{ cm}^{-1})$ and at 30 °C and 600 rpm (pulsed with 10 s on and 10 s off and a low force setting) with a Varioskan LUX multimode microplate reader. Assays were performed with four separate samples and with no-enzyme control reactions. Assays were done in a total volume of 200 μ L containing 140 μ L of 0.1 M sodium phosphate buffer (pH 7.0), 10 μL of 20 mM sodium phosphite (Na₂HPO₃·5H₂O final concentration 1 mM), 40 μ L of PTDH (final concentrations: 0.03 μ M for His-SpyT-PTDH-SnoopT, 0.05 μ M for His-PTDH, and 0.25 µM for the much less active His-SnoopC-PTDH-SpyC), and 10 μ L of 5 mM NADP⁺ (final concentration 250 μ M). For the determination of kinetic parameters, either the concentration of NADP+ or sodium phosphite was fixed in the assay at a concentration of 0.25 mM or 1 mM, respectively, and the concentrations of the second substrate varied from 0.02 to 1 mM for Na₂HPO₃ or 0.005-0.25 mM for NADP+. All reactions were started with the addition of NADP+ and were performed in four replicates. Kinetic parameters were calculated using the Michaelis-Menten fitting function of Origin (version 2022b) (Table 2).

P450BM3m NADPH Coupling Efficiency. To determine the NADPH coupling efficiency, reactions were performed as described above with 0.4 µM P450BM3m, 1 mM indole or lauric acid, and 1 mM NADPH in 0.1 M sodium phosphate buffer (pH 7.0) at 30 °C. For indole, 200 μ L reactions were followed spectrophotometrically at 340 and 670 nm until complete consumption of NADPH after 1.5 h. The coupling efficiency for indole was then calculated as the percentage of indoxyl (two molecules of indoxyl form one molecule of indigo) relative to the consumed NADPH. For lauric acid, 1 mL reactions were carried out for 1.5 h (30 °C, 180 rpm) and reactions stopped by adding 10% (v/v) saturated NaCl H₂SO₄ (6 g NaCl in 10 mL 50% H₂SO₄). Lauric acid hydroxylation products were then identified and quantified following extraction and derivatization by GC mass spectrometry (GC-MS) and a GC-FID as described below. The coupling efficiency was calculated as the percentage of produced hydroxylauric acid products relative to that of consumed NADPH. All assays were performed with four separate samples.

P450BM3m and PTDH Cross-Linking to EutM Scaffolds. Cross-linking of P450BM3m and PTDH cargo proteins individually or combined to EutM scaffolds was confirmed by SDS-PAGE (Figures 7b and S16) as described for GFP cargo above except that the molar ratio of enzyme cargo to the isopeptide bond-forming EutM partner was increased to 1:4. Scaffolds and enzymes were mixed in 0.1 M sodium phosphate buffer (pH 7.0) at 30 °C for 1 h before loading onto a gel. Individual enzyme immobilization reactions contained the following final concentrations: 15 μM His-SpyT-P450BM3m-SnoopT (1.9 mg/mL) or 15 μ M His-SpyT-PTDH-SnoopT (0.7 mg/mL) mixed with 60 μM His-SpyC-EutM-SnoopC (2.0 mg/mL) or 60 μM SpyC-EutM-SnoopC in hybrid scaffolds His-EutM:SpyC-EutM-SnoopC = 3.9:1 (4.7 mg/ mL) or His-EutM:SpyC-EutM-SnoopC = 8.8:1 (8.0 mg/mL). For coimmobilization, 15 µM His-SpyT-P450BM3m-SnoopT

(1.9 mg/mL) or 15 μ M His-SpyT-PTDH-SnoopT (0.7 mg/mL) (30 μ M total enzyme cargo) was mixed with 120 μ M SpyC-EutM-SnoopC in hybrid scaffold His-EutM:SpyC-EutM-SnoopC = 8.8:1 (16 mg/mL). This coimmobilized sample was also analyzed with TEM as described above (Figures 8a and S20). Enzyme or scaffold-only reactions served as controls for SDS-PAGE analysis.

Effect of Scaffold Immobilization on P450BM3m Activity and Stability. To assess the effect of scaffold attachment on P450BM3m activity (Figures 7c and S17), 20 µM P450BM3m (dual-modified and unmodified as control, 2.5 mg/mL) was mixed at a 1:4 molar ratio with 80 μ M His-SpyC-EutM-SnoopC (2.7 mg/mL) in 0.1 M sodium phosphate buffer (pH 7.0). This mixture was then quickly diluted with the same buffer to achieve final enzyme concentrations ranging from 0.5, 1.0, 2.0, 8.0, 16.0, to 20 μ M followed by 1 h incubation at 30 $^{\circ}$ C and 180 rpm for cross-linking. A 40 μ L reaction mixture was then taken out from each sample to quantify specific and volumetric P450BM3m activities in 200 μ L assays, as described above, by monitoring both NADPH oxidation and indigo formation with 0.25 mM NADPH and 2.5 mM indole. The final P450BM3m concentrations in the assays (after 5x dilution) ranged from 0.1 to 4 μ M. Note that NADPH oxidation could not be quantified in assays containing 1.6 µM or higher enzyme concentrations as NADPH was completely consumed after 30 s.

To compare the effect of scaffold type on P450BM3m activity (Figure 7d), 8 µM His-P450BM3m (1.0 mg/mL) or His-SpyT-P450BM3m-SnoopT (1.0 mg/mL) was mixed with 32 μ M His-SpyC-EutM-SnoopC (1.1 mg/mL) or 32 μ M SpyC-EutM-SnoopC in His-EutM:SpyC-EutM-SnoopC = 3.9:1 (2.5 mg/mL) or His-EutM:SpyC-EutM-SnoopC = 8.8:1 (4.3 mg/mL) and incubated for 1 h at 30 °C and 180 rpm, and the specific activity for indigo measured with 40 μ L of reaction mixture (final P450BM3m concentration, 1.6 μ M (0.2 mg/mL) in assay) as described above. To determine the effect of scaffolds on P450BM3m stability (Figure S18), the above reaction mixtures were incubated at 30 $^{\circ}$ C and 40 μ L samples removed at 0-168 h for measurement of specific activity and indigo formation, as described above. All measurements were performed with four replicates for each enzyme immobilization reaction. Control reactions contained no scaffolds.

Effect of Scaffold Immobilization on PTDH Activity and Stability. To determine the effect of the hybrid scaffold on PTDH activity, 0.5 μM His-PTDH or His-SpyT-PTDH-SnoopT (0.02 mg/mL) was mixed at a molar ration of 1:4 with $2 \mu M$ His-SpyC-EutM-SnoopC (0.07 mg/mL) or $2 \mu M$ SpyC-EutM-SnoopC in His-EutM:SpyC-EutM-SnoopC = 3.9:1 (0.2) mg/mL) or His-EutM:SpyC-EutM-SnoopC = 8.8:1 (0.3 mg/ mL) and incubated within 0.1 M sodium phosphate buffer (pH 7.0) at 30 °C and 180 rpm for 1 h. A 40 μL reaction mixture was then assayed in a 200 μL assay to determine the specific PTDH activity as described above with 1 mM sodium phosphite and 0.25 mM NADP+ in 0.1 M sodium phosphate buffer (pH 7.0) (Figure 7d). The effect of scaffolds on PTDH stability was measured by incubating the reaction mixtures for up to 168 h at 30 $^{\circ}$ C and removing 40 μ L samples after set time intervals for specific activity measurements. All measurements were performed with four replicates for each enzyme immobilization reaction. Control reactions contained no scaffolds (Figure S19).

Implementation of the Coupled Reaction System with Free P450BM3m and PTDH. To test and optimize the coupled P450BM3m-PTDH system for indole or lauric acid conversion, reactions were performed with fixed PTDH and ratios of P450BM3m for the conversion of 2.5 mM indole or lauric acid (Figure 8b). For indigo conversion, indigo formation was quantified spectrophotometrically (see kinetic assay above) after 15 min at 30 °C (600 rpm) in 200 μ L reactions containing 20 μ L of 100 mM sodium phosphite (final concentration 10 mM), 10 µL of 5 mM NADP+ (final concentration 0.25 mM), 2 µL of 250 mM indole in DMSO (final concentration 2.5 mM), and 40 μ L of enzyme mixture with 8 μ M (0.3 mg/mL) His-PTDH and 2, 4, or 8 μ M (0.2-1.0 mg/mL) His-P450BM3m (final concentration 1.6 μ M His-PTDH; 0.4, 0.8, or 1.6 μ M His-P450BM3m) in 0.1 M sodium phosphate buffer (pH 7.0). For lauric acid conversion, hydroxylauric acid formation was quantified by a GC-FID (see GC analysis below) after 15 min at 30 °C (180 rpm) in 1 mL reactions containing 100 μ L of 100 mM sodium phosphite (final concentration 10 mM), 50 µL of 5 mM NADP+ (final concentration 0.25 mM), 80 µL of 31.25 mM lauric acid in DMSO (final concentration 2.5 mM), and 200 μ L of enzyme mixture with 8 µM His-PTDH and 2, 4, or 8 µM His-P450BM3m (final concentration 1.6 µM His-PTDH; 0.4, 0.8, or 1.6 μ M His-P450BM3m) in 0.1 M sodium phosphate buffer (pH 7.0). Higher enzyme concentrations were also tested for hydroxylauric acid formation by conducting reactions under the same conditions with equimolar concentrations (1.6, 3.2, 6.4, 12.8, or 25.6 μ M) of P450BM3m and PTDH (Figure S22). All assays were performed with four separate samples.

Influence of P450BM3m and NADPH Concentrations on Indole Oxidation. To characterize inhibition of indigo formation by high P450BM3m and NADPH concentration (Figure S21), P450BM3m spectrophotometric assays were performed (see above) with 0.25 or 3.5 mM NADPH and with either 0.4 or 1.6 μ M (0.05 or 0.2 mg/mL) His-P450BM3m or His-SpyT-P450BM3m-SnoopT. Indigo formation was monitored and quantified at 670 nm after 20 min at 30 °C. Assays were performed with four separate samples.

Scaffolded P450BM3m-PTDH Reaction System for **Lauric Acid Conversion.** Small-scale reactions (1 mL) with both enzymes were set up with and without (control) scaffolds to characterize effects on the conversion (Figure 8c). For this, $6.4 \mu M$ His-SpyT-P450BM3m-SnoopT (0.8 mg/mL) and 6.4μM His-SpyT-PTDH-SnoopT (0.3 mg/mL) were mixed at a 1:4 molar ratio of enzymes to cross-linking scaffold building blocks with 51.2 µM His-SpyC-EutM-SnoopC (1.8 mg/mL) or 51.2 µM SpyC-EutM-SnoopC in His-EutM:SpyC-EutM-SnoopC = 3.9:1 (4.0 mg/mL) or in His-EutM:SpyC-EutM-SnoopC = 8.8:1 (6.9 mg/mL) hybrid scaffolds. The mixtures were then incubated at 30 °C and 180 rpm for 1 h to allow for cross-link formation. Conversions were then performed in 1 mL reactions by mixing 500 μ L of the scaffolded enzymes (or enzymes only control) with 270 μ L of 0.1 M sodium phosphate buffer (pH 7.0), 100 µL of 100 mM sodium phosphite (final concentration 10 mM), 80 μ L of 31.25 mM lauric acid in DMSO (final concentration 2.5 mM), and 50 μ L of 5 mM NADP+ (final concentration 0.25 mM), to start the reactions. The final P450BM3m and PTDH concentrations were 3.2 μ M. After 10 min of incubation at 30 °C and 180 rpm, reactions were stopped (see assay for coupling efficiency) and lauric acid hydroxylation products extracted and quantified

(see below). All reactions were performed with four separate samples.

For larger-scale conversion reactions (5 mL) with 20% (v/v) dodecane (Figure 8d) followed over 24 h, 1.6 µM His-SpyT-P450BM3m-SnoopT (0.2 mg/mL) and 6.4 µM His-SpyT-PTDH-SnoopT (0.3 mg/mL) were first mixed with 20 µM hybrid His-EutM:SpyC-EutM-SnoopC = 8.8:1 (2.7 mg/mL) (or without scaffolds as control) and incubated at 30 °C and 180 rpm for 1 h to allow for the coimmobilization of enzymes and cross-linking of scaffolds. Conversion reactions were then performed in 5 mL reactions by mixing 2.5 mL of the scaffolded enzymes (or enzymes only control) with 1.4 mL of 0.1 M sodium phosphate buffer (pH 7.0), 0.5 mL of 0.5 M sodium phosphite (final concentration 50 mM), 0.1 mL of DMSO [final concentration 2% (v/v)], and 1 mL of 100 mM lauric acid in dodecane [final lauric acid concentration 20 mM and 20% (v/v) dodecane]. Reactions were started with 0.5 mL of 5 mM NADP+ (final concentration 0.5 mM). The final enzyme concentrations in the reactions were 0.8 µM His-SpyT-P450BM3m-SnoopT and 3.2 μ M His-SpyT-PTDH-SnoopT. After 0.5, 1, 3, 6, 9, 12, and 24 h incubation at 30 $^{\circ}$ C and 120 rpm, 100 and 20 μ L aliquots were removed from the aqueous and dodecane phases, respectively, and combined. Reactions were stopped (see assay for coupling efficiency) for the quantification of lauric acid conversion products (see below). All reactions were performed with four separate samples.

Recycling of Scaffold-Coimmobilized P450BM3m and PTDH for Lauric Acid Conversion. Dual-modified P450BM3m and PTDH (6.4 µM each) were first coimmobilized onto hybrid EutM:His-SpyC-EutM-SnoopC scaffolds at a 1:4 molar ratio of enzymes to the cross-linking scaffold building block as described above. For the first reaction cycle, conversions were performed in 3 mL reactions by mixing 1.5 mL of the scaffolded enzymes with 0.81 mL of 0.1 M sodium phosphate buffer (pH 7.0), 0.3 mL of 0.1 M sodium phosphite (final concentration 10 mM), and 0.24 mL of 31.25 mM lauric acid in DMSO [final lauric acid concentration 2.5 mM and 8% (v/v) DMSO]. Reactions were started with 0.15 mL of 5 mM NADP⁺ (final concentration of 0.25 mM). The final enzyme concentrations in the reactions were 3.2 µM His-SpyT-P450BM3m-SnoopT and 3.2 μ M His-SpyT-PTDH-SnoopT. After 30 min incubation at 30 °C and 180 rpm, a 100 μ L aliquot was removed for the quantification of lauric acid conversion products (see below). Another 100 µL was removed to measure the protein concentration for SDS-PAGE analysis (Figure S23). The remaining sample was spun down at 5000g for 5 min at 4 °C to recover the scaffolded enzymes. After the supernatant was removed, the material was reused under the same conditions and in the same volume for the next reaction cycle. All reactions were performed with four separate samples.

GC Analysis of Lauric Acid Hydroxylation. Stopped enzyme reaction samples were extracted twice with an equal volume of ethyl acetate. The organic extracts were collected, and 10 μ L of 10 mM of palmitic acid (corresponding to 1 mM after derivatization) was added as an internal reference prior to evaporation and resuspension in 50 μ L of dimethylformamide (DMF). Resuspended samples were then derivatized for GC analysis with 50 μ L of BSTFA with 1% N,O-bis(trimethylsilyl)-trifluoroacetamide with 1% trimethylchlorosilane (MilliporeSigma, Burlington, MA, USA) at 60 °C for 30 min. For quantification by GC analysis of hydroxylauric acid products

and the lauric acid substrate, derivatization reactions were similarly performed with 1 mM palmitic acid (as an internal reference) and 0.01–2 mM 12-hydroxylauric acid or 0.01–1 mM lauric acid in 50 μ L of DMF to calculate detector response factors for derivatized monohydroxylauric acids and lauric acid. Peak areas of all hydroxylated lauric acid products were combined to quantify the hydroxylation activity of P450BM3m.

Derivatized samples were then analyzed and quantified using an Agilent 6890 Plus gas chromatograph with a FID and equipped with a capillary column (HP-5 ms, 30 m \times 0.25 mm \times 0.25 μ m, Agilent, Santa Clara, CA, USA) with the following parameters: The FID heater temperature was set to 320 °C and flow rates for H₂, air, and make up gas (helium) were 40, 450, and 45 mL/min, respectively. A representative GC-FID chromatogram with retention times of derivatized fatty acids is shown in Figure S24.

To identify derivatized lauric acid oxidation products of samples, GC-MS was performed with an Agilent 7890A GC system and a 5975C MSD detector equipped with a capillary column (HP-5 ms, 30 m × 0.25 mm × 0.25 μ m, Agilent, Santa Clara, CA, USA) with the following parameters: 1 μ L injection volume with a 300 °C port temperature and a split ratio of 10; helium as a carrier gas and a temperature gradient from 40 to 300 °C with 5 °C/min and a 10 min isothermal hold at 300 °C and a 8 min solvent delay. Representative fragmentation spectra of derivatized 9-, 10-, and 11-hydroxylauric acids are shown in Figure S25 and matched reported spectra ^{19,67} and the expected sequence of retention times.

Statistical Analysis and Reproducibility. Enzyme kinetic parameters were calculated by using the Hill or Michaelis-Menten fitting function in Origin (version 2022b). R-squared values were >0.95. Standard curves for hydroxylauric acid (R-squared values ≥0.99) and EutM protein densitometry (R-squared value >0.9) analysis were created in Microsoft Excel 365 using the linear trendline function. Mean and standard deviations were calculated using the Average and STDEV functions in Microsoft Excel 365. The yield, molar ratios, and insoluble and soluble fractions of hybrid scaffolds were measured in triplicate with protein isolated from three independent recombinant cultures per scaffold expression construct. All scaffold proteins and enzymes were purified at least three times to isolate sufficient quantities for all of the experiments. Cross-linking experiments for PAGE analysis and microscopy were done at least twice to obtain representative gel and microscopy images. All enzyme reactions were performed as four separate replicate samples.

ASSOCIATED CONTENT

Supporting Information

The Supporting Information is available free of charge at https://pubs.acs.org/doi/10.1021/acssynbio.4c00587.

Native PAGE analysis, SDS-PAGE analysis, TEM images, DLS and AUC analysis, scaffold stability analysis, fluorescence microscopy images, enzyme activity and stability analysis, biocatalyst reuse, GC and GC-MS analysis, and tables of RBS sequence, hydroxylauric acid product profiles, plasmids, strains, amino acid sequence, and nucleotide sequences (PDF)

AUTHOR INFORMATION

Corresponding Author

Claudia Schmidt-Dannert — Department of Biochemistry, Molecular Biology & Biophysics, University of Minnesota, Minneapolis, Minnesota 55455, United States; BioTechnology Institute, University of Minnesota, Saint Paul, Minnesota 55108, United States; orcid.org/0000-0002-0559-3656; Phone: +1 612 625 5782; Email: schmi232@umn.edu

Authors

Ruijie Zhang — Department of Biochemistry, Molecular Biology & Biophysics, University of Minnesota, Minneapolis, Minnesota 55455, United States; BioTechnology Institute, University of Minnesota, Saint Paul, Minnesota 55108, United States; orcid.org/0000-0001-7892-3516

Sun-Young Kang — Department of Biochemistry, Molecular Biology & Biophysics, University of Minnesota, Minneapolis, Minnesota 55455, United States; BioTechnology Institute, University of Minnesota, Saint Paul, Minnesota 55108, United States; orcid.org/0000-0002-1327-0160

François Gaascht — Department of Biochemistry, Molecular Biology & Biophysics, University of Minnesota, Minneapolis, Minnesota 55455, United States; BioTechnology Institute, University of Minnesota, Saint Paul, Minnesota 55108, United States; orcid.org/0000-0001-6129-0708

Eliana L. Peña — Department of Biochemistry, Molecular Biology & Biophysics, University of Minnesota, Minneapolis, Minnesota 55455, United States; BioTechnology Institute, University of Minnesota, Saint Paul, Minnesota 55108, United States

Complete contact information is available at: https://pubs.acs.org/10.1021/acssynbio.4c00587

Author Contributions

§R.Z and S.-Y.K. contributed equally to this work. R.Z. contributed to the experimental design, created genetic constructs, isolated and characterized scaffolds, performed microscopy and enzyme assays, analyzed the data, and wrote the manuscript. S.-Y.K. contributed to the experimental design, isolation of proteins, microscopy analysis of the scaffolds, DLS and AUC analysis, analysis of the data, and writing of the manuscript. F.G. contributed to the GC analysis and manuscript writing. E.L.P. contributed to the design and construction of plasmids and the writing of the manuscript. C.S.-D. conceived, devised, conceptualized, and directed the overall project, analyzed the data, and wrote the manuscript together with R.Z. and S.-Y.K.

Notes

The authors declare no competing financial interest. All data generated or analyzed in this study are included in this manuscript and accompanying Supporting Information. Plasmids created in this study can be made available subject to an MTA that can be requested by contacting the corresponding author Prof. Schmidt-Dannert (schmi232@umn.edu), who will respond to requests within a week. The Protein Data Bank data set (PDB: 3I6P) was used to generate EutM hexamer structure representation in Figures 1 and 2.

ACKNOWLEDGMENTS

This research was sponsored by grants from the National Science Foundation (CBET-1916030), the Department of

Energy Advanced Research Project Agency (ARPA-E) (DE-AR0001510), and the BioTechnology Institute at the University of Minnesota. We thank Dr. Matthew Johnson (University of Minnesota) and Prof. Borries Demeler (University of Lethbridge) for their assistance and expertise in AUC analysis.

REFERENCES

- (1) Miserez, A.; Yu, J.; Mohammadi, P. Protein-based biological materials: molecular design and artificial production. *Chem. Rev.* **2023**, 123 (5), 2049–2111.
- (2) Seo, M.-J.; Schmidt-Dannert, C. Organizing multi-enzyme systems into programmable materials for biocatalysis. *Catalysts* **2021**, *11* (4), 409.
- (3) Wallin, K.; Zhang, R.; Schmidt-Dannert, C. Programmable self-assembling protein nanomaterials: Current status and prospects. In *Engineered Living Materials*; Srubar Iii, W. V., Ed.; Springer International Publishing: Cham, 2022; pp 51–94.
- (4) Shen, Y.; Levin, A.; Kamada, A.; Toprakcioglu, Z.; Rodriguez-Garcia, M.; Xu, Y.; Knowles, T. P. J. From protein building blocks to functional materials. *ACS Nano* **2021**, *15* (4), 5819–5837.
- (5) Kortemme, T. De novo protein design—From new structures to programmable functions. *Cell* **2024**, *187* (3), 526–544.
- (6) Mout, R.; Bretherton, R. C.; Decarreau, J.; Lee, S.; Gregorio, N.; Edman, N. I.; Ahlrichs, M.; Hsia, Y.; Sahtoe, D. D.; Ueda, G.; Sharma, A.; Schulman, R.; DeForest, C. A.; Baker, D. De novo design of modular protein hydrogels with programmable intra- and extracellular viscoelasticity. *Proc. Natl. Acad. Sci. U.S.A.* **2024**, *121* (6), No. e2309457121.
- (7) Hilditch, A. T.; Romanyuk, A.; Cross, S. J.; Obexer, R.; McManus, J. J.; Woolfson, D. N. Assembling membraneless organelles from de novo designed proteins. *Nat. Chem.* **2024**, *16* (1), 89–97.
- (8) Zhang, W.; Mo, S.; Liu, M.; Liu, L.; Yu, L.; Wang, C. Rationally designed protein building blocks for programmable hierarchical architectures. *Front. Chem.* **2020**, *8*, 587975.
- (9) Hirschi, S.; Ward, T. R.; Meier, W. P.; Müller, D. J.; Fotiadis, D. Synthetic biology: Bottom-up assembly of molecular systems. *Chem. Rev.* **2022**, *122* (21), 16294–16328.
- (10) Ben-Sasson, A. J.; Watson, J. L.; Sheffler, W.; Johnson, M. C.; Bittleston, A.; Somasundaram, L.; Decarreau, J.; Jiao, F.; Chen, J.; Mela, I.; Drabek, A. A.; Jarrett, S. M.; Blacklow, S. C.; Kaminski, C. F.; Hura, G. L.; De Yoreo, J. J.; Kollman, J. M.; Ruohola-Baker, H.; Derivery, E.; Baker, D. Design of biologically active binary protein 2D materials. *Nature* **2021**, *589* (7842), 468–473.
- (11) Bolivar, J. M.; Woodley, J. M.; Fernandez-Lafuente, R. Is enzyme immobilization a mature discipline? Some critical considerations to capitalize on the benefits of immobilization. *Chem. Soc. Rev.* **2022**, *51* (15), 6251–6290.
- (12) Pokhrel, A.; Kang, S.-y.; Schmidt-Dannert, C. Ethanolamine bacterial microcompartments: from structure, function studies to bioengineering applications. *Curr. Opin. Microbiol.* **2021**, *62*, 28–37.
- (13) Zhang, G.; Schmidt-Dannert, S.; Quin, M. B.; Schmidt-Dannert, C. Protein-based scaffolds for enzyme immobilization. *Methods Enzymol.* **2019**, *617*, 323–362.
- (14) Zhang, G.; Quin, M. B.; Schmidt-Dannert, C. Self-assembling protein scaffold system for easy *in vitro* coimmobilization of biocatalytic cascade enzymes. *ACS Catal.* **2018**, 8 (6), 5611–5620.
- (15) Kang, S.-Y.; Pokhrel, A.; Bratsch, S.; Benson, J. J.; Seo, S.-O.; Quin, M. B.; Aksan, A.; Schmidt-Dannert, C. Engineering *Bacillus subtilis* for the formation of a durable living biocomposite material. *Nat. Commun.* **2021**, *12* (1), 7133.
- (16) Zhang, G.; Johnston, T.; Quin, M. B.; Schmidt-Dannert, C. Developing a protein scaffolding system for rapid enzyme immobilization and optimization of enzyme functions for biocatalysis. *ACS Synth. Biol.* **2019**, *8* (8), 1867–1876.
- (17) Veggiani, G.; Nakamura, T.; Brenner, M. D.; Gayet, R. V.; Yan, J.; Robinson, C. V.; Howarth, M. Programmable polyproteams built

- using twin peptide superglues. *Proc. Natl. Acad. Sci. U.S.A.* **2016**, 113 (5), 1202–1207.
- (18) Manea, F.; Garda, V. G.; Rad, B.; Ajo-Franklin, C. M. Programmable assembly of 2D crystalline protein arrays into covalently stacked 3D bionanomaterials. *Biotechnol. Bioeng.* **2020**, *117* (4), 912–923.
- (19) Beyer, N.; Kulig, J. K.; Bartsch, A.; Hayes, M. A.; Janssen, D. B.; Fraaije, M. W. P450(BM3) fused to phosphite dehydrogenase allows phosphite-driven selective oxidations. *Appl. Microbiol. Biotechnol.* **2017**, *101* (6), 2319–2331.
- (20) Whitehouse, C. J. C.; Bell, S. G.; Wong, L.-L. P450BM3 (CYP102A1): connecting the dots. *Chem. Soc. Rev.* **2012**, *41* (3), 1218–1260.
- (21) Chen, Z.; Wu, T.; Yu, S.; Li, M.; Fan, X.; Huo, Y.-X. Self-assembly systems to troubleshoot metabolic engineering challenges. *Trends Biotechnol.* **2024**, 42, 43–60.
- (22) Caparco, A. A.; Dautel, D. R.; Champion, J. A. Protein mediated enzyme immobilization. *Small* **2022**, *18* (19), 2106425.
- (23) Jäger, V. D.; Kloss, R.; Grünberger, A.; Seide, S.; Hahn, D.; Karmainski, T.; Piqueray, M.; Embruch, J.; Longerich, S.; Mackfeld, U.; Jaeger, K. E.; Wiechert, W.; Pohl, M.; Krauss, U. Tailoring the properties of (catalytically)-active inclusion bodies. *Microb. Cell Factories* **2019**, *18* (1), 33.
- (24) Kowalski, A. E.; Johnson, L. B.; Dierl, H. K.; Park, S.; Huber, T. R.; Snow, C. D. Porous protein crystals as scaffolds for enzyme immobilization. *Biomater. Sci.* **2019**, *7* (5), 1898–1904.
- (25) Diener, M.; Kopka, B.; Pohl, M.; Jaeger, K.-E.; Krauss, U. Fusion of a coiled-coil domain facilitates the high-level production of catalytically active enzyme inclusion bodies. *ChemCatChem* **2016**, 8 (1), 142–152.
- (26) Yin, L.; Guo, X.; Liu, L.; Zhang, Y.; Feng, Y. Self-assembled multimeric-enzyme nanoreactor for robust and efficient biocatalysis. *ACS Biomater. Sci. Eng.* **2018**, 4 (6), 2095–2099.
- (27) Ledesma-Fernandez, A.; Velasco-Lozano, S.; Santiago-Arcos, J.; Lopez-Gallego, F.; Cortajarena, A. L. Engineered repeat proteins as scaffolds to assemble multi-enzyme systems for efficient cell-free biosynthesis. *Nat. Commun.* **2023**, *14* (1), 2587.
- (28) Woodley, J. M. Ensuring the Sustainability of Biocatalysis. *ChemSusChem* **2022**, *15* (9), No. e202102683.
- (29) Pédelacq, J. D.; Cabantous, S.; Tran, T.; Terwilliger, T. C.; Waldo, G. S. Engineering and characterization of a superfolder green fluorescent protein. *Nat. Biotechnol.* **2006**, 24 (1), 79–88.
- (30) Noël, C. R.; Cai, F.; Kerfeld, C. A. Purification and characterization of protein nanotubes assembled from a single bacterial microcompartment shell subunit. *Adv. Mater. Interfaces* **2016**, 3 (1), 1500295.
- (31) Kaczmarczyk, A.; Vorholt, J. A.; Francez-Charlot, A. Cumate-inducible gene expression system for sphingomonads and other alphaproteobacteria. *Appl. Environ. Microbiol.* **2013**, 79 (21), 6795–6802.
- (32) Salis, H. M.; Mirsky, E. A.; Voigt, C. A. Automated design of synthetic ribosome binding sites to control protein expression. *Nat. Biotechnol.* **2009**, 27 (10), 946–950.
- (33) Seo, S. O.; Schmidt-Dannert, C. Development of a synthetic cumate-inducible gene expression system for *Bacillus. Appl. Microbiol. Biotechnol.* **2019**, *103* (1), 303–313.
- (34) Vick, J. E.; Johnson, E. T.; Choudhary, S.; Bloch, S. E.; Lopez-Gallego, F.; Srivastava, P.; Tikh, I. B.; Wawrzyn, G. T.; Schmidt-Dannert, C. Optimized compatible set of BioBrick vectors for metabolic pathway engineering. *Appl. Microbiol. Biotechnol.* **2011**, 92, 1275–1286.
- (35) Faulkner, M.; Zhao, L. S.; Barrett, S.; Liu, L. N. Self-assembly stability and variability of bacterial microcompartment shell proteins in response to the environmental change. *Nanoscale Res. Lett.* **2019**, *14*, 54.
- (36) Schmidt-Dannert, S.; Zhang, G.; Johnston, T.; Quin, M. B.; Schmidt-Dannert, C. Building a toolbox of protein scaffolds for future immobilization of biocatalysts. *Appl. Microbiol. Biotechnol.* **2018**, *102* (19), 8373–8388.

- (37) Fansher, D. J.; Besna, J. N.; Fendri, A.; Pelletier, J. N. Choose your own adventure: A comprehensive database of reactions catalyzed by cytochrome P450 BM3 variants. *ACS Catal.* **2024**, *14*, 5560–5592.
- (38) Valikhani, D.; Bolivar, J. M.; Dennig, A.; Nidetzky, B. A tailormade, self-sufficient and recyclable monooxygenase catalyst based on coimmobilized cytochrome P450 BM3 and glucose dehydrogenase. *Biotechnol. Bioeng.* **2018**, *115* (10), 2416–2425.
- (39) Solé, J.; Caminal, G.; Schürmann, M.; Alvaro, G.; Guillén, M. Co-immobilization of P450 BM3 and glucose dehydrogenase on different supports for application as a self-sufficient oxidative biocatalyst. *J. Chem. Technol. Biotechnol.* **2019**, 94 (1), 244–255.
- (40) Maurer, S. C.; Schulze, H.; Schmid, R. D.; Urlacher, V. Immobilisation of P450 BM-3 and an NADP+ cofactor recycling system: Towards a technical application of heme-containing monooxygenases in fine chemical synthesis. *Adv. Synth. Catal.* **2003**, 345 (6–7), 802–810.
- (41) Valikhani, D.; Bolivar, J. M.; Pelletier, J. N. An overview of cytochrome P450 immobilization strategies for drug metabolism studies, biosensing, and biocatalytic applications: Challenges and opportunities. *ACS Catal.* **2021**, *11* (15), 9418–9434.
- (42) Bahrami, A.; Iliuta, I.; Garnier, A.; Larachi, F.; Vincent, T.; Iliuta, M. C. Kinetics of enzymatic hydroxylation by free and MNPs-immobilized NADH-dependent cytochrome P450 BM3 from *Bacillus megaterium*. *Ind. Eng. Chem. Res.* **2019**, 58 (2), 808–815.
- (43) Buergler, M. B.; Dennig, A.; Nidetzky, B. Process intensification for cytochrome P450 BM3-catalyzed oxy-functionalization of dodecanoic acid. *Biotechnol. Bioeng.* **2020**, 117 (8), 2377–2388.
- (44) Li, Q.-S.; Schwaneberg, U.; Fischer, P.; Schmid, R. D. Directed evolution of the fatty-acid hydroxylase P450 BM-3 into an indole-hydroxylating catalyst. *Chem. Eur. J.* **2000**, 6 (9), 1531–1536.
- (45) Appel, D.; Lutz-Wahl, S.; Fischer, P.; Schwaneberg, U.; Schmid, R. D. A P450BM-3 mutant hydroxylates alkanes, cycloalkanes, arenes and heteroarenes. *J. Biotechnol.* **2001**, 88 (2), 167–171.
- (46) Maurer, S. C.; Kühnel, K.; Kaysser, L. A.; Eiben, S.; Schmid, R. D.; Urlacher, V. B. Catalytic hydroxylation in biphasic systems using CYP102A1 mutants. *Adv. Synth. Catal.* **2005**, 347 (7–8), 1090–1098.
- (47) Woodyer, R.; Zhao, H.; van der Donk, W. A. Mechanistic investigation of a highly active phosphite dehydrogenase mutant and its application for NADPH regeneration. *FEBS J* **2005**, 272 (15), 3816–3827.
- (48) Beyer, N.; Kulig, J. K.; Fraaije, M. W.; Hayes, M. A.; Janssen, D. B. Exploring PTDH-P450BM3 variants for the synthesis of drug metabolites. *ChemBioChem* **2018**, *19* (4), 326-337.
- (49) Huang, W.-C.; Westlake, A. C. G.; Maréchal, J.-D.; Joyce, M. G.; Moody, P. C. E.; Roberts, G. C. K. Filling a hole in cytochrome P450 BM3 improves substrate binding and catalytic efficiency. *J. Mol. Biol.* **2007**, *373* (3), *633*–651.
- (50) Li, Q.-S.; Ogawa, J.; Schmid, R. D.; Shimizu, S. Indole hydroxylation by bacterial cytochrome P450 BM-3 and modulation of activity by cumene hydroperoxide. *Biosci., Biotechnol., Biochem.* **2005**, 69 (2), 293–300.
- (51) Rowlatt, B.; Yorke, J. A.; Strong, A. J.; Whitehouse, C. J. C.; Bell, S. G.; Wong, L.-L. Chain length-dependent cooperativity in fatty acid binding and oxidation by cytochrome P450BM3 (CYP102A1). *Protein Cell* **2011**, 2 (8), 656–671.
- (52) Kong, F.; Chen, J.; Qin, X.; Liu, C.; Jiang, Y.; Ma, L.; Xu, H.; Li, S.; Cong, Z. Evolving a P450BM3 peroxygenase for the production of indigoid dyes from indoles. *ChemCatChem* **2022**, *14* (24), No. e202201151.
- (53) Mendoza-Avila, J.; Chauhan, K.; Vazquez-Duhalt, R. Enzymatic synthesis of indigo-derivative industrial dyes. *Dyes Pigm.* **2020**, *178*, 108384
- (54) Jeffreys, L. N.; Pacholarz, K. J.; Johannissen, L. O.; Girvan, H. M.; Barran, P. E.; Voice, M. W.; Munro, A. W. Characterization of the structure and interactions of P450 BM3 using hybrid mass spectrometry approaches. *J. Biol. Chem.* **2020**, 295 (22), 7595–7607.
- (55) Cirino, P. C.; Arnold, F. H. Regioselectivity and activity of cytochrome P450 BM-3 and mutant F87A in reactions driven by hydrogen peroxide. *Adv. Synth. Catal.* **2002**, *344* (9), 932–937.

- (56) Vidal-Limón, A.; Águila, S.; Ayala, M.; Batista, C. V.; Vazquez-Duhalt, R. Peroxidase activity stabilization of cytochrome P450BM3 by rational analysis of intramolecular electron transfer. *J. Inorg. Biochem.* **2013**, *122*, 18–26.
- (57) Bahrami, A.; Vincent, T.; Garnier, A.; Larachi, F.; Boukouvalas, J.; Iliuta, M. C. Noncovalent immobilization of optimized bacterial cytochrome P450 BM3 on functionalized magnetic nanoparticles. *Ind. Eng. Chem. Res.* **2017**, *56* (39), 10981–10989.
- (58) Nöth, M.; Hussmann, L.; Belthle, T.; El-Awaad, I.; Davari, M. D.; Jakob, F.; Pich, A.; Schwaneberg, U. MicroGelzymes: pH-independent immobilization of cytochrome P450 BM3 in microgels. *Biomacromolecules* **2020**, *21* (12), 5128–5138.
- (59) Xia, Y.; Li, K.; Li, J.; Wang, T.; Gu, L.; Xun, L. T5 exonuclease-dependent assembly offers a low-cost method for efficient cloning and site-directed mutagenesis. *Nucleic Acids Res.* **2019**, 47 (3), No. e15.
- (60) Studier, F. W. Protein production by auto-induction in high density shaking cultures. *Protein Expression Purif.* **2005**, 41 (1), 207–234.
- (61) Starr lab Quantification of protein bands using densitometry. https://sites.google.com/a/umn.edu/starrlab/protocols/quantitation/quantification-of-protein-bands-using-densitometry (accessed may 1, 2022).
- (62) Demeler, B. Methods for the design and analysis of sedimentation velocity and sedimentation equilibrium experiments with proteins. *Curr. Protoc. Protein Sci.* **2010**, *60* (1), 7 13 1–7 13 24.
- (63) Brookes, E.; Cao, W.; Demeler, B. A two-dimensional spectrum analysis for sedimentation velocity experiments of mixtures with heterogeneity in molecular weight and shape. *Eur. Biophys. J.* **2010**, 39 (3), 405–414.
- (64) Demeler, B.; van Holde, K. E. Sedimentation velocity analysis of highly heterogeneous systems. *Anal. Biochem.* **2004**, 335 (2), 279–288
- (65) Omura, T.; Sato, R. The carbon monoxide-binding pigment of liver microsomes. J. Biol. Chem. 1964, 239 (7), 2379–2385.
- (66) Ebert, M. C. C. J. C.; Guzman Espinola, J.; Lamoureux, G.; Pelletier, J. N. Substrate-specific screening for mutational hotspots using biased molecular dynamics simulations. *ACS Catal.* **2017**, 7 (10), 6786–6797.
- (67) Tooker, B. C.; Kandel, S. E.; Work, H. M.; Lampe, J. N. *Pseudomonas aeruginosa* cytochrome P450 CYP168A1 is a fatty acid hydroxylase that metabolizes arachidonic acid to the vasodilator 19-HETE. *J. Biol. Chem.* **2022**, 298 (3), 101629.